

# The SHMS 11GeV/c Spectrometer in Hall C at Jefferson Lab

S. Ali<sup>a</sup>, G.R. Ambrose<sup>b</sup>, A. Asaturyan<sup>c</sup>, V. Berdnikov<sup>a</sup>, P. Brindza<sup>d</sup>, R. Carlini<sup>1,\*</sup>, M. Carmignotto<sup>a</sup>, A. Dittmann<sup>g</sup>, D. Dutta<sup>e</sup>, R. Ent<sup>d</sup>, H. Fenker<sup>d</sup>, M. Fowler<sup>d</sup>, W. Henry<sup>d</sup>, N. Hlavin<sup>a</sup>, T. Horn<sup>a,d</sup>, G.M. Huber<sup>b,1</sup>, Y. Illieva<sup>f</sup>, S.J.D. Kay<sup>b</sup>, V. Kumar<sup>b</sup>, S. Lassiter<sup>d</sup>, W.B. Li<sup>b</sup>, A. Mkrtchyan<sup>a</sup>, H. Mkrtchyan<sup>c</sup>, P. Nadel-Turonski<sup>d</sup>, I. Pegg<sup>a</sup>, A. Ramos<sup>h</sup>, J. Reinhold<sup>h</sup>, I. Sapkota<sup>a</sup>, B. Sawatzky<sup>d</sup>, V. Tadevosyan<sup>c</sup>, R.L. Trotta<sup>a</sup>, S. Zhamkochyan<sup>c</sup>, S. A. Wood<sup>d</sup>

<sup>a</sup>The Catholic University of America, Washington, DC 20064, USA

<sup>b</sup>University of Regina, Regina, Saskatchewan S4S 0A2, Canada

<sup>c</sup>A. I. Alikhanyan National Science Laboratory, Yerevan 0036, Armenia

<sup>d</sup>Thomas Jefferson National Accelerator Facility, Newport News, Virginia 23606, USA

<sup>e</sup>Mississippi State University, Mississippi State, Mississippi 39762, USA

<sup>f</sup>University of South Carolina, Columbia, South Carolina 29208, USA

<sup>g</sup>University of Illinois, Urbana-Champaign, Illinois, USA

<sup>h</sup>Florida International University, University Park, Florida 33199, USA

---

## Abstract

The *Super High Momentum Spectrometer* (SHMS) has been built for Hall C at the Thomas Jefferson National Accelerator Facility (Jefferson Laboratory). With a momentum capability reaching 11 GeV/c, the SHMS provides measurements of secondary charged particles produced in electron scattering experiments using the maximum available beam energy from the upgraded Jefferson Lab accelerator. The SHMS is an ion-optics magnetic spectrometer comprised of a series of new superconducting magnets which transport charged particles through an array of triggering, tracking, and particle-identification detectors that measure momentum, energy, angle and position in order to allow kinematic reconstruction of the events back to their origin at the scattering target. The detector system is protected from background radiation by a sophisticated shielding enclosure. The entire spectrometer is mounted on a rotating support structure which allows measurements to be taken with a large acceptance over laboratory scattering angles from 5.5° to 40°, thus allowing a wide range of low cross-section experiments to be conducted. These will complement and extend the previous Hall C research program to higher energies.

**Keywords:** Magnetic spectrometer, Electron scattering, Tracking detectors, Particle identification, Electron calorimetry, Radiation shielding.

---

## 1. Introduction

### 1.1. Jefferson Lab Overview

The Continuous Electron Beam Accelerator Facility at Thomas Jefferson National Accelerator Facility (Jefferson Lab) provides high energy electron beams for fundamental nuclear physics experiments. Originally planned for maximum electron beam energies of 4 GeV, the accelerator operated at energies of up to 6 GeV starting in 2000. An upgrade of the facility was recently completed in 2017, enabling beam delivery at a maximum energy of 12 GeV to the new experimental Hall D, and 11 GeV to the existing Halls, A, B, and C.

The electron beam at Jefferson Lab operates at high duty cycle, with beam repetition rates of 249.5 or 499 MHz delivered to the experimental halls. High beam polarization (> 80%) is also routinely available.

In the 6 GeV era, Halls A, B, and C executed a large program of experiments focusing primarily on elucidating the quark-gluon structure of nucleons and nuclei. Experimental Hall B made use of a large acceptance spectrometer capable of detecting many-body final states over a large region of kinematic phase space in one setting. Halls A and C made use of magnetic focusing spectrometers. In Hall A, the two High Resolution Spectrometers (HRS) emphasized excellent momentum resolution. In Hall C, the Short Orbit Spectrometer (SOS) facilitated the detection of short-lived final states (pions and kaons) at modest momentum while

---

\*Corresponding author

<sup>1</sup><http://orcid.org/0000-0002-5658-1065>

the High Momentum Spectrometer was capable of detecting particles up the maximum beam energy at Jefferson Lab.

As part of the 12 GeV Upgrade at Jefferson Lab, a new experimental hall, Hall D, was built to search for gluonic excitations in the meson spectrum using a photon beam produced via coherent Bremsstrahlung. The GlueX experiment in Hall D began commissioning in 2014 and has taken production-quality data since 2016.

The existing Halls A, B, and C were also upgraded as part of the 12 GeV Upgrade. The Hall A beamline and beam polarimeters were upgraded to accommodate operation at 11 GeV. Hall A has made use of the existing HRS spectrometers in its early 12 GeV era experiments (which began initial data-taking in 2014) and plans to install specialized, dedicated equipment for future measurements. Experimental Hall B replaced its large acceptance CLAS spectrometer with the new CLAS-12 spectrometer. This new spectrometer retains the key features of large acceptance and robust particle identification over a large momentum range but with more emphasis on particle detection in the forward direction, required due to the higher beam energies. Finally, Hall C replaced its Short Orbit Spectrometer with the new Super-High Momentum Spectrometer (SHMS). This new spectrometer was designed guided by experience from the 6 GeV program, with the goal of serving as an optimal partner to the HMS for coincidence experiments.

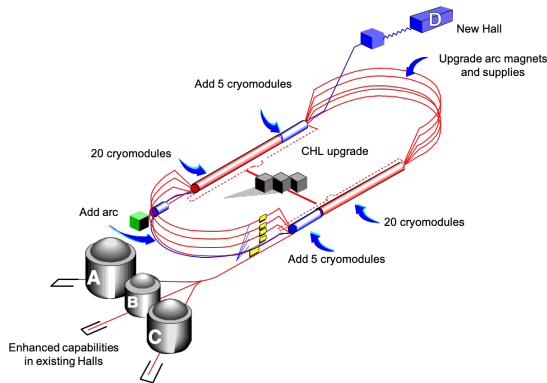


Figure 1: Schematic of hall and accelerator improvements as part of Jefferson Lab 12 GeV Upgrade.

### 1.2. Hall C Experimental Program at 6 GeV

The HMS and SOS spectrometers in Hall C enabled the execution of a diverse program of experiments. The well-understood acceptance of both spectrometers,

in tandem with excellent kinematic reproducibility allowed the extraction of precise cross sections. A particular strength was the control of point-to-point systematic uncertainties, which allowed high precision Rosenbluth, or L-T, separations. Examples of inclusive cross section measurements, using primarily the HMS, are shown in Figs. 2 and 3.

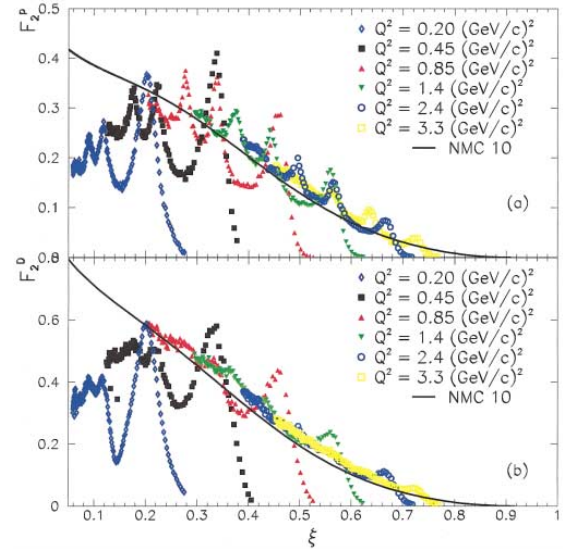


Figure 2: Inclusive  $F_2$  structure functions measured in the resonance region compared to a DIS fit. When plotted vs. the Nachtmann variable  $\xi$ , the DIS fit agrees, on average, with the resonance region data, demonstrating quark-hadron duality [4].

In addition, the small minimum angle (10.5 degrees) accessible with the HMS allowed the execution of pion electroproduction experiments, where, in many cases, the pion is emitted in the forward direction. This allowed the successful execution of a program of measurements of the pion form factor [71, 72], which also incorporates precise L-T separations, as well measurements of charged pion production in Semi-inclusive Deep Inelastic Scattering (SIDIS) [73] (see Figs. 4 and 5).

The high momentum reach of the HMS (up to the available beam energy of 6 GeV) enabled measurements of the  $A(e, e'p)$  process to large  $Q^2$  [74, 75] to look for signs of Color Transparency as well measurements of inclusive electron scattering at  $x > 1$  to access contributions of “superfast” quarks to inelastic structure functions [76] and measure the relative contributions of Short Range Correlations (SRCs) in the nuclear wave function [77].

The experiments noted above are just a sample of the

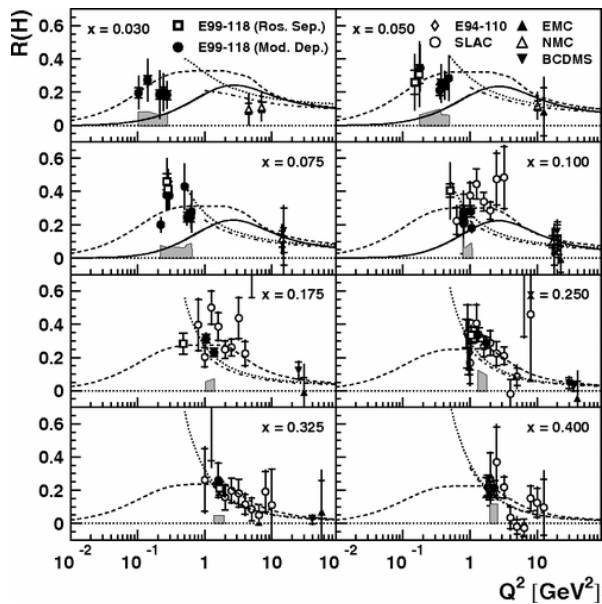


Figure 3: Measurement of  $R = \frac{\sigma_L}{\sigma_T}$  at low  $Q^2$ . The extraction of  $R$  requires precise L-T separations with excellent control of point-to-point systematic uncertainties. Figure from [70].

89  $\approx 30$  “standard equipment” experiments that were executed in the 6 GeV era in Hall C. Other experiments include measurements of exclusive kaon production, resonance ( $\Delta$ ,  $S_{11}$ ) production, color transparency via pion electroproduction, and numerous inclusive electron scattering measurements using hydrogen and deuterium, as well as heavier nuclear targets. In some cases, the HMS was paired with dedicated equipment for special measurements. Examples of this include measurement of the ratio of elastic proton form factors ( $G_E/G_M$ ) to large  $Q^2$ , as well as measurements using a dynamically polarized  $\text{NH}_3$ .

### 101 1.3. Hall C 12 GeV Program

102 The new, Super-High Momentum Spectrometer was designed to build on the experimental capabilities exploited during the Hall C program at higher energies. Notably, this includes:

- 106 1. Excellent kinematic control reproducibility
- 107 2. Thorough understanding of spectrometer acceptance
- 108 3. Small angle capability (down to 5.5 degrees) for detection of forward mesons
- 109 4. Central momentum up to (nearly) the maximum beam energy accessible in Hall C
- 110 5. In-plane and out-of-plane acceptance well matched to the existing HMS to facilitate experiments detecting two particle in coincidence

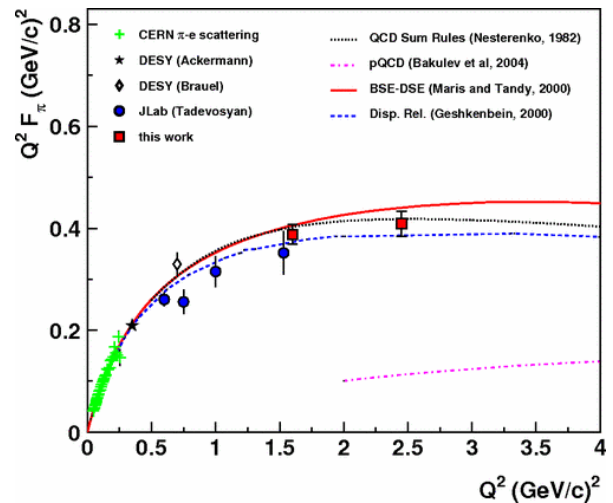


Figure 4: Measurements of the charged pion form factor in Hall C (6 GeV era). Extraction of the pion form factor requires a precise L-T separation, as well as detection of the charged pion at small forward angles. Figure from [72].

116 Several “commissioning” experiments were chosen for the first year of 12 GeV running in Hall C to exercise the above requirements as much as possible. These experiments ran in 2018 and will be discussed briefly below.

121 The first such experiment was a measurement of inclusive electron scattering cross sections from hydrogen and deuterium [56]. Such a cross section experiment is an excellent testing ground for understanding of the spectrometer acceptance, while not pushing the SHMS performance in other areas. Some settings for this experiment were chosen to allow simultaneous measurement with the well-understood HMS to provide a cross section. In addition, some time was devoted to the measurement of inclusive cross section ratios for nuclear targets relative to deuterium [57]. These ratios are well-measured for certain nuclei and serve as another straightforward verification of the spectrometer acceptance due to the need to compare yields from extended (10 cm long) targets to shorter, solid targets (mm scale).

136 An extension of the 6 GeV color transparency experiments to larger  $Q^2$  [59] served as an excellent first experiment with which to exercise the SHMS in coincidence mode. In this  $A(e, e'p)$  experiment, there are few random coincidences so isolating the coincidence reaction is straightforward. This experiment, as well as a measurement of deuteron electro-disintegration [58], also tested the high momentum capabilities of the SHMS. The SHMS was used at momenta larger than 8.5 GeV/c for these experiments. Although the max-

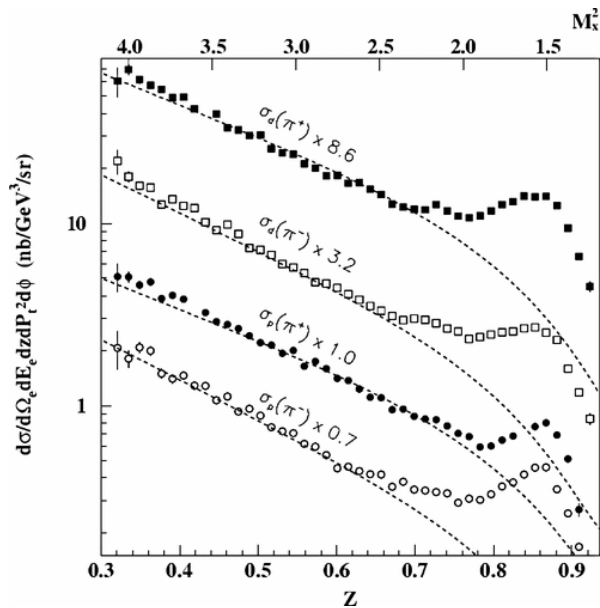


Figure 5: Cross sections for semi-inclusive  $\pi^+$  and  $\pi^-$  production from hydrogen and deuterium. The cross sections are compared to a parameterization that uses fragmentation functions fit to high energy  $e^+e^-$  collisions. Figure from [73].

imum central momentum of the SHMS is almost 11 GeV, 8.5 GeV/c was already sufficient to learn about the performance of the superconducting magnets and spectrometer optics when pushed to a significant fraction of the spectrometer's ultimate capabilities. In addition, the body of  $H(e, e'p)$  data acquired for both these initial coincidence experiments served to provide constraints the experiment kinematics, allowing one to test the possible variation of, *e.g.* the spectrometer pointing or central momentum for various settings.

A set of meson electroproduction experiments followed the initial commissioning experiments and further exercised the SHMS capabilities. Two of the experiments measured charged pion electroproduction in semi-inclusive deep inelastic scattering [60, 61]. The SHMS was used at central angles smaller than  $7^\circ$  for the SIDIS running. An additional challenge was the relatively high singles rates in the SHMS. Both experiments aim at making precise measurements of  $\pi^+/\pi^-$  ratios so control of rate dependent systematic effects is a key challenge. The third experiment [42] measured exclusive cross sections for  $K^+$  production above the resonance region, in particular, extracting the longitudinal and transverse cross sections via a Rosenbluth separation. In this case, the experimental uncertainties are expected to be dominated by statistics, so this serves as an excellent candidate for an a first L-T separation since the

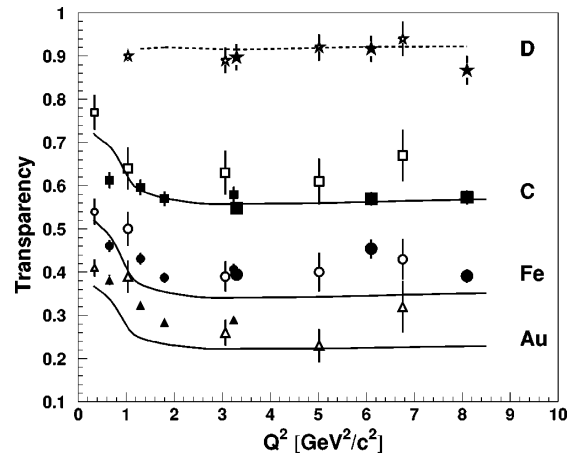


Figure 6: Measurement of transparency for  $(e, e'p)$ . Solid points are from (6 GeV era) Hall C measurements [74, 75]. At the largest  $Q^2$ , the HMS momentum is  $> 5$  GeV. Figure from [75].

systematic requirements are less stringent. In common with the charged pion SIDIS experiments, the kaon experiment required use of the SHMS at small angles and had to face the challenge of high singles rates.

The “year-1” experiments described above give a sense of the SHMS capabilities important for the overall physics program. More recent experiments include measurements of  $J/\Psi$  photoproduction, Virtual Compton Scattering, measurement of the charged pion factor at very low  $Q^2$ , and inclusive electron scattering from polarized  $^3\text{He}$  to extract  $A_1^n$  and  $d_2^n$ . In the near future, measurements of the EMC Effect and at  $x > 1$  (in both the inclusive and exclusive channels) from a variety of nuclei as well L-T separated  $\pi^+$  cross sections (to extract the charged pion factor and measure the cross section scaling behavior at large  $Q^2$ ) are planned. Further in the future, additional L-T separations in inclusive scattering (to measure  $R = \frac{\sigma_L}{\sigma_T}$  from hydrogen, deuterium, and several nuclei) and semi-inclusive reactions (to make the first precise measurement of  $R$  for the SIDIS reaction) are also planned. While not all future experiments will make use of the SHMS, it is a key component of the Hall C 12 GeV experimental program.

## 2. Specifications for the upgraded Hall-C Spectrometer complex

The physics outlined in the previous section can be accessed only if the Hall C spectrometer system is capable of providing the necessary measurements with precision, rate, and trigger capabilities consistent with those physics goals. Originally, Hall C offered the

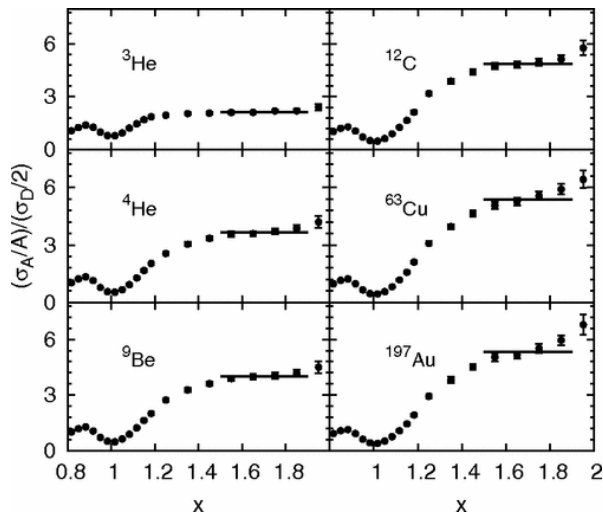


Figure 7: Measurements of cross section ratios for nuclear targets relative to deuterium at  $x > 1$ . The size of the ratio is proportional to the relative contributions of 2-nucleon Short Range Correlations to the nuclear wave function. These measurements required high momentum in the HMS. Figure from [77].

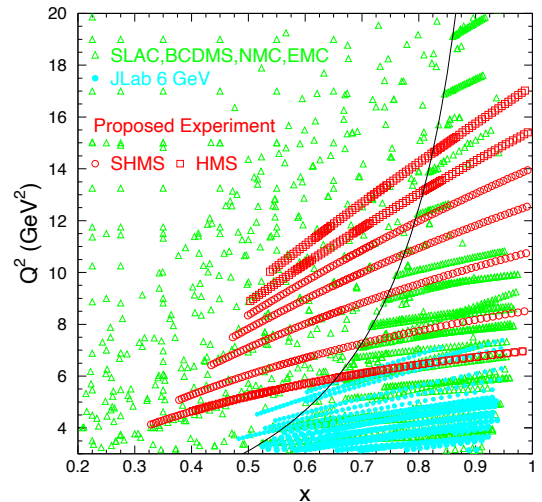


Figure 8: Kinematic coverage of  $F_2$  measurements from experiment E12-10-002 [56], which measured inclusive electron scattering cross sections as part of Hall C's 12 GeV commissioning experiments.

203 7.4 GeV/c High Momentum Spectrometer (HMS) and  
 204 its lower-momentum (1.8 GeV/c) partner, the Short-  
 205 Orbit Spectrometer (SOS). These two devices were uti-  
 206 lized independently by some experiments and in coin-  
 207 cidence by others. The performance specifications for  
 208 the SHMS were drafted such that the SHMS-HMS pair  
 209 would provide similar complimentary functions in the  
 210 higher-momentum regime. That is, the SHMS was de-  
 211 veloped as a general-purpose spectrometer with prop-  
 212 erties similar to the existing HMS, but with a higher  
 213 maximum momentum capability (11 GeV/c). The 11 GeV/c  
 214 limit of the SHMS was selected because the accelera-  
 215 tor constrained maximum beam energy to any of the first  
 216 generation endstations (A, B, C) is 11 GeV/c. Table 1  
 217 summarizes the demonstrated performance of the HMS  
 218 and the design specifications for the SHMS.

219 With the higher beam energies in use at Jefferson Lab  
 220 after the 12-GeV Upgrade, scattered electrons and sec-  
 221 ondary particles are boosted to more forward directions.  
 222 Thus the SHMS acceptance is made to extend down to  
 223 a  $5.5^\circ$  scattering angle, and needs to cover angles  
 224 no higher than  $40^\circ$ . Nevertheless, high energies gen-  
 225 erally lead to smaller cross sections. Therefore preci-  
 226 sion experiments can be performed only if a spectrom-  
 227 eter provides large overall acceptance, high rate capa-  
 228 bility, and precise momentum measurement. As shown  
 229 in Table 1, the SHMS design includes a momentum bite  
 230 even larger than the HMS, and achieves an angular ac-  
 231 ceptance within a factor of two of its low-energy part-

232  
233  
234  
235  
236  
237  
238  
239

ner. The combination of dispersive optics and preci-  
 sion tracking provides excellent momentum resolution.  
 Triggering, data-acquisition, and particle identifica-  
 tion rates are the same or better than those of the HMS.  
 This performance is achieved not only through the use  
 of faster, modern electronics, but also by innovative ra-  
 diation shielding that reduces the background flux seen  
 by the detectors.

### 3. Design and Development of the SHMS Systems

241 In this section we present design details and data  
 242 demonstrating the performance of each the SHMS sub-  
 243 systems. The entire spectrometer is carried on a steel  
 244 support structure which can rotate through an arc on the  
 245 left side of the beam-line in Hall C. Like the HMS car-  
 246 riage, it is secured to a central pivot so that it rotates  
 247 around a vertical axis that intersects the electron beam-  
 248 line at the experimental target. This is shown in Fig. 11.

249 Acceptance at the smallest scattering angles is en-  
 250 abled by the presence of a horizontal-bending dipole as  
 251 the first element in the magnetic optical system. This  
 252 small deflection moves the subsequent pieces of the  
 253 SHMS farther from the beamline, relaxing the size con-  
 254 straints on the other magnetic elements (described in  
 255 Section 3.1) and shielding (Section 3.2). The shielded  
 256 enclosure is itself a technically-optimized combination  
 257 of concrete, lead, boron, and plastic. It surrounds the  
 258 detectors and the electronics of the control and data-  
 259 acquisition systems.

<i>Parameter</i>	<i>HMS Performance</i>	<i>SHMS Specification</i>
Range of Central Momentum	0.4 to 7.4 GeV/c	2 to 11 GeV/c
Momentum Acceptance	$\pm 10\%$	-10% to +22%
Momentum Resolution	0.1% – 0.15%	0.03% – 0.08%
Scattering Angle Range	10.5° to 90°	5.5° to 40°
Target Length Accepted at 90°	10 cm	25 cm
Horizontal Angle Acceptance	$\pm 32$ mrad	$\pm 18$ mrad
Vertical Angle Acceptance	$\pm 85$ mrad	$\pm 45$ mrad
Solid Angle Acceptance	8.1 msr	4 msr
Horizontal Angle Resolution	0.8 mrad	0.5 – 1.2 mrad
Vertical Angle Resolution	1.0 mrad	0.3 – 1.1 mrad
Target resolution ( $y_{tar}$ )	0.3 cm	0.1 - 0.3 cm
Maximum Event Rate	4–5 kHz	4–5 kHz
Max. Flux within Acceptance	$\sim 5$ MHz	$\sim 5$ MHz
e/h Discrimination	>1000:1 at 98% efficiency	>1000:1 at 98% efficiency
$\pi/K$ Discrimination	100:1 at 95% efficiency	100:1 at 95% efficiency

Table 1: Demonstrated Performance of the HMS and Design Specifications for the SHMS. Resolutions are quoted at 1 sigma.

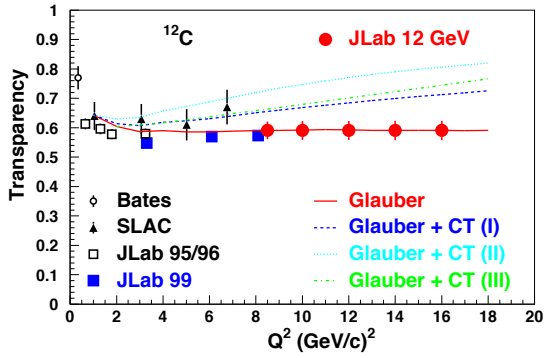


Figure 9: Projected uncertainties for the measurement of color transparency [59]. This measurement served as the first coincidence measurement in the 12 GeV era in Hall C.

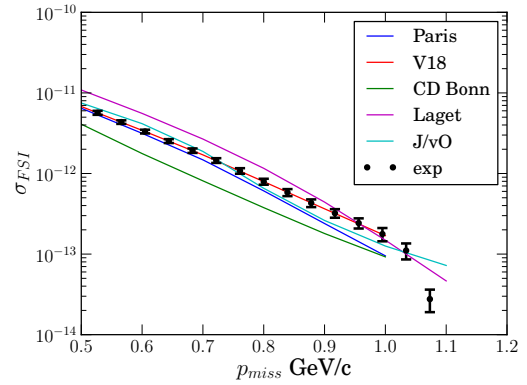


Figure 10: Projected uncertainties for the measurement of deuteron electrodisintegration at large missing momentum [58] (Hall C commissioning experiment).

260 Basic trigger information comes from four planes  
261 of scintillator or quartz-bar hodoscopes. Tracking is  
262 provided by twelve planes of conventional drift cham-  
263 bers, and particle identification uses gas and aerogel  
264 Cherenkov counters, a preshower counter, and a total-  
265 absorption shower counter. The detector system details  
266 are presented in sections 3.3 through 3.9. Details of the  
267 event-triggering schemes, the data-acquisition system,  
268 and software appear in sections 4 and 5.

### 269 3.1. Magnetic Optics

270 The SHMS consists of five magnets used to deter-  
271 mine the momentum, angles and position of particles  
272 scattered from the target using their angle and posi-  
273 tion measurements by the SHMS detectors. The first  
274 is a dipole magnet which bends the incident particles  
275 in the horizontal plane. A quadrupole triplet provides  
276 a point-to-point focus. To optimize acceptance in the  
277 vertical scattering plane, the first quadrupole focuses in

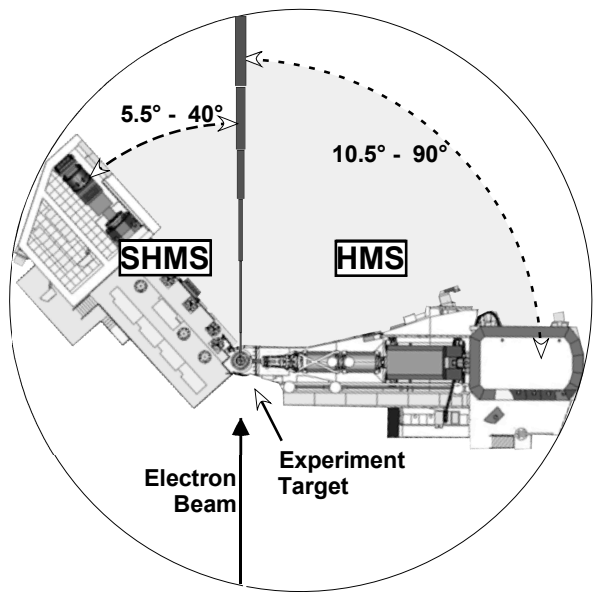


Figure 11: Simplified Plan View of Hall C showing the footprints of the SHMS and HMS. The SHMS occupies the smaller side of Hall C, where the smaller, low-momentum Short-Orbit Spectrometer (SOS) had been previously located.

278 the vertical while the second quadrupole defocuses and  
 279 the third quadrupole focuses. A vertical-bending dipole  
 280 magnet follows the last quadrupole and disperses parti-  
 281 cles with different momenta across the focal plane. In  
 282 point-to-point optics, all particles with the same mo-  
 283 mentum will be displaced by the same vertical distance  
 284 in the focal plane.

### 3.1.1. The Magnets and Vacuum Channel

286 A specially-design horizontal-bend dipole (HB) pre-  
 287 cedes the first quadrupole. Its purpose is to provide an  
 288 initial 3° separation between scattered particles and the  
 289 electron beam so that particles scattered at small angles  
 290 can be accepted.

291 As shown in Fig. 11, in order to fit within the space  
 292 available in Hall C the SHMS must be even shorter  
 293 than its lower-momentum partner, the HMS. All of the  
 294 SHMS magnets are superconducting so that they can  
 295 provide the necessary large bending and focusing effects  
 296 in short distances. Given the small-angle acceptance re-  
 297 quirement, the HB and the first two quadrupoles (Q1  
 298 and Q2) must have special provisions to provide clear-  
 299 ance for the electron beam and its vacuum pipe. HB  
 300 is a “C”-magnet so that all of the flux-return iron is on  
 301 the side away from the beamline. The front of the HB  
 302 cryostat, between the beamline and the magnet bore,  
 303 is made very narrow. Both Q1 and Q2 have notches  
 304 in their cryostats and iron yokes so that they, too, can

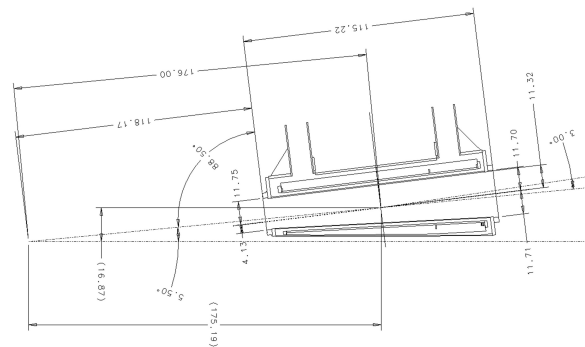


Figure 12: Top view schematic of the horizontal bender (HB) magnet with dimensions given in units of cm. The center of the HB magnet is at 5.5° for the beam line and 176 cm from the hall center.

305 clear the beamline when the spectrometer is configured  
 306 at small scattering angles. Yoke steel for Q1 is inside  
 307 the cryostat. The final quadrupole (Q3) and the dipole  
 308 ( $D_{SHMS}$ ) have external warm yokes. Parameters of the  
 309 SHMS magnets are provided in Table 2. Details about  
 310 the design and construction of the SHMS magnets can  
 311 be found in [3].

312 To minimize multiple scattering as particles pass  
 313 through the SHMS, the bores of all of the magnets are  
 314 evacuated. The vacuum space begins at a window on  
 315 the front of HB. The entrance window into HB is ap-  
 316 proximately 15 cm square and is made of 0.01 inch thick  
 317 aluminum. A vacuum connection is made between the  
 318 exit of HB and Q1 entrance which is followed by the  
 319 40 cm diameter vacuum bore in Q1. The exit of Q1  
 320 is connected to the entrance of Q2 by a vacuum pipe.  
 321 The vacuum vessel bore through Q2, Q3, and  $D_{SHMS}$   
 322 is 60 cm in diameter. The location of the end of the  
 323 vacuum after the exit of  $D_{SHMS}$  depends on the needs  
 324 of the experiment. If the experiment needs the Noble  
 325 Gas Cherenkov (NGC) detector (described in Sec. 3.7,  
 326 then a window is placed at the exit of  $D_{SHMS}$  with the  
 327 NGC detector placed between the exit window and the  
 328 drift chambers. Otherwise, a Vacuum Extension Tank  
 329 (VET) is attached to the exit of the  $D_{SHMS}$  that puts the  
 330 exit window at 30 cm from the first drift chamber in the  
 331 detector stack. In both cases, the dipole exit window is  
 332 made of 0.020 inch thick aluminum.

### 3.1.2. Optics

The relative strengths of the integral fields of the  
 magnets are set to maximize acceptance while at the  
 same time optimizing resolution in momentum and scat-  
 tering angle. The transport of a particle with the relative  
 momentum,  $\delta = \frac{p-p_c}{p_c}$ , from the target to midway be-

<i>Parameter</i>	<i>HB</i>	<i>Q1</i>	<i>Q2</i>	<i>Q3</i>	<i>D<sub>SHMS</sub></i>
Max Field or Gradient	2.6 T	7.9 T/m	11.8 T/m	7.9 T/m	3.9 T
Effective Field Length	0.80 m	1.9 m	1.6 m	1.6 m	2.9 m
Current at 11 GeV/c	3923 A	2322 A	3880 A	2553 A	3510 A
Aperture	14.5x18 cm	40 cm	60 cm	60 cm	60 cm

Table 2: Parameters of the SHMS Magnets

tween the two set drift chambers in the focal plane of the SHMS can be characterized by an optics matrix. The particle momentum is  $p$  and the central momentum of the spectrometer is  $p_c$ . The particle starts with the vertical and horizontal positions ( $x_{tar}$  and  $y_{tar}$ ) and angles ( $x'_{tar} = \frac{\Delta x_{tar}}{\Delta z_{tar}}$  and  $y'_{tar} = \frac{\Delta y_{tar}}{\Delta z_{tar}}$ ) in the  $z_{tar} = 0$  plane. These positions and angles are measured relative to the central ray of the spectrometer. After magnetic transport, it arrives at the focal plane with the vertical and horizontal positions ( $x_{fp}$  and  $y_{fp}$ ) and angles ( $x'_{fp}$  and  $y'_{fp}$ ). The first order optics matrix is

$$\begin{pmatrix} x_{fp} \\ x'_{fp} \\ y_{fp} \\ y'_{fp} \end{pmatrix} = \begin{pmatrix} -1.5 & 0.0 & 0.0 & 0.0 & 1.65 \\ -0.5 & -0.7 & 0.0 & 0.0 & 3.2 \\ 0.0 & 0.0 & -1.9 & -0.2 & -0.1 \\ 0.0 & 0.0 & -3.0 & -0.8 & 0.1 \end{pmatrix} \begin{pmatrix} x_{tar} \\ x'_{tar} \\ y_{tar} \\ y'_{tar} \\ \delta \end{pmatrix} \quad (1)$$

The units of the positions, angles and  $\delta$  are in centimeters, milliradians and %.

The acceptance of the spectrometer is mainly determined by the collimator that is placed between the HB magnet and the first quadrupole. A remotely-operated collimator box is installed on the SHMS between the HB and Q1 magnets. The collimator ladder assembly within this box may be positioned at three settings. The top position (accessed when the assembly is at its lowest position) is a stretched octagon with opening height 9.843" and width 6.693" on the upstream side. It is 2.5" thick. The lower two positions both present sieve holes in rectangular pattern with holes separated by 0.6457" horizontally and 0.9843" vertically. The sieve pattern at the middle ladder position has 11 columns of holes with the sixth column centered horizontally. The holes on the bottom sieve are in ten columns and are offset by one-half a column gap from those in the middle sieve. The sieve collimators are 1.25" thick. The geometry is illustrated in Fig. 13. Both sieves and octagonal collimator are made of Mi-Tech™ Tungsten HD-17 (Density 17 g/cc, 90% W, 6% Ni, 4% Cu).

To determine the vertical size of the collimator studies were done with SNAKE (magnet transport code). Without the collimator, the vertical acceptance is mainly

determined by the mechanical exit of the HB magnet. The vertical size of  $\pm 12.5$  cm was chosen to match this vertical cut-off to maximize the acceptance. Two vertical sizes of  $\pm 8$  cm and  $\pm 10.5$  cm for the collimators were studied. A plot of the acceptance each collimator versus  $\delta$  is shown in Figure 14. The acceptance drops from an average of 4 msr for  $\pm 12.5$  cm to an average of 3 msr for  $\pm 8$  cm. Another consideration minimizing the loss of events in the bore of the vertical dipole after they pass the entrance of the dipole. A plot in Figure 14 shows the fraction of events which make it to the focal plane. The number of events lost in the dipole bore as a function of  $\delta$  is reduced by decreasing the vertical height of the collimator. With the  $\pm 12.5$  cm collimator, the fraction of events making to the focal plane drops to 75% at  $\delta = 0.15$ . The decision was made to use the  $\pm 12.5$  cm vertical opening to maximize the solid angle acceptance of the SHMS at the expense of increased reliance on the understanding the losses in the SHMS dipole bore.

A magnetic transport code, SNAKE, was used to model the acceptance of the SHMS. The mechanical sizes of the magnets and magnet field maps from TOSCA are used to create a model of the SHMS in SNAKE. The acceptance of the SHMS versus  $\delta$  determined by SNAKE is plotted in Fig. 15. A separate calculation is done using the Hall C Monte Carlo (SIMC) which uses COSY transport matrix. The acceptance of the SHMS versus  $\delta$  determined by SIMC is plotted in Fig. 15. The agreement between the two calculations is excellent.

The reconstruction of a particle's momentum, horizontal target position and vertical and horizontal angles from the focal plane positions and angles can also be represented by an optics matrix. Each event calculates the target interaction point from the tracks reconstructed in the focal plane using the drift chamber information. Target offsets, beam offsets and spectrometer mis-pointings are accounted for separately when reconstructing events. The optics matrix elements consist of a set of coefficients and the values of the powers for each focal plane element. The coefficients for each fo-

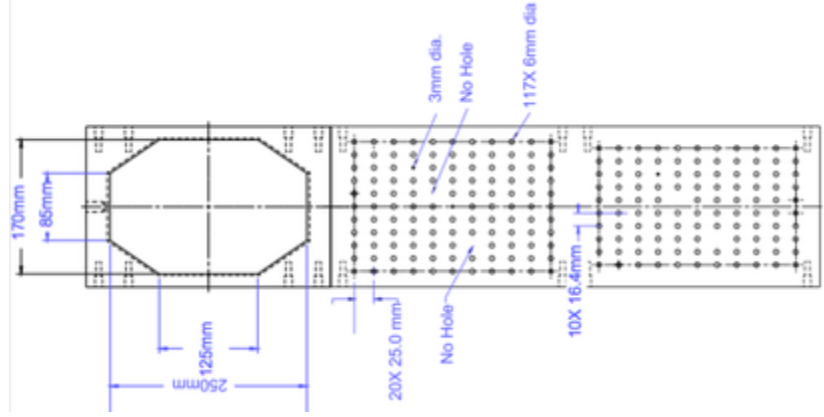


Figure 13: SHMS collimator

401 cal plane variable are  $X'$ ,  $Y$ ,  $Y'$ , and  $D$ , and the powers  
 402 of each focal plane variable are represented by  $ijklm$ .  
 403 The powers for each term range from zero to six with  
 404 the sum of the powers for a given term not exceeding  
 405 six. The reconstruction equations for the target quanti-  
 406 ties are written as shown in Eq. 2.

$$\begin{aligned}
 x'_{tar} &= \sum_{ijklm} X'_{ijklm} x_{fp}^i x'_{fp}{}^j y_{fp}^k y'_{fp}{}^l x_{tar}^m \\
 y_{tar} &= \sum_{ijklm} Y_{ijklm} x_{fp}^i x'_{fp}{}^j y_{fp}^k y'_{fp}{}^l x_{tar}^m \\
 y'_{tar} &= \sum_{ijklm} Y'_{ijklm} x_{fp}^i x'_{fp}{}^j y_{fp}^k y'_{fp}{}^l x_{tar}^m \\
 \delta &= \sum_{ijklm} D_{ijklm} x_{fp}^i x'_{fp}{}^j y_{fp}^k y'_{fp}{}^l x_{tar}^m
 \end{aligned} \tag{2}$$

407 From Eq. 2, it can be seen that the target reconstruc-  
 408 tion is actually under-determined. For each event, there  
 409 are four givens ( $x_{fp}$ ,  $y_{fp}$ ,  $x'_{fp}$ ,  $y'_{fp}$ ) and five unknowns to  
 410 solve for ( $x_{tar}$ ,  $y_{tar}$ ,  $x'_{tar}$ ,  $y'_{tar}$ , and  $\delta$ ).  $x_{tar}$  is never directly  
 411 measured, but it is reconstructed with the knowledge of  
 412 the beam position and reconstructed values of  $y_{tar}$ ,  $x'_{tar}$ ,  
 413  $y'_{tar}$ . The  $x_{tar}$  dependent coefficients are used directly  
 414 from COSY calculations with the reconstructed  $x'_{tar}$  and  
 415  $\delta$  being most sensitive to knowledge of  $x_{tar}$ . To account  
 416 for  $x_{tar}$ , an iterative procedure is done where first the  
 417  $y_{tar}$ ,  $x'_{tar}$ ,  $y'_{tar}$  and  $\delta$  are calculated by setting  $x_{tar}$  equal  
 418 to the vertical beam position. Then  $x_{tar}$  is calculated us-  
 419 ing the vertical beam position,  $y_{tar}$ ,  $x'_{tar}$  and  $y'_{tar}$  and the  
 420 reconstruction matrix is recalculated with the new  $x_{tar}$ .  
 421 This is repeated in a loop until the change in  $x'_{tar}$  com-  
 422 pared to the previous iteration is less than 2 mr for no  
 423 more than five iterations.

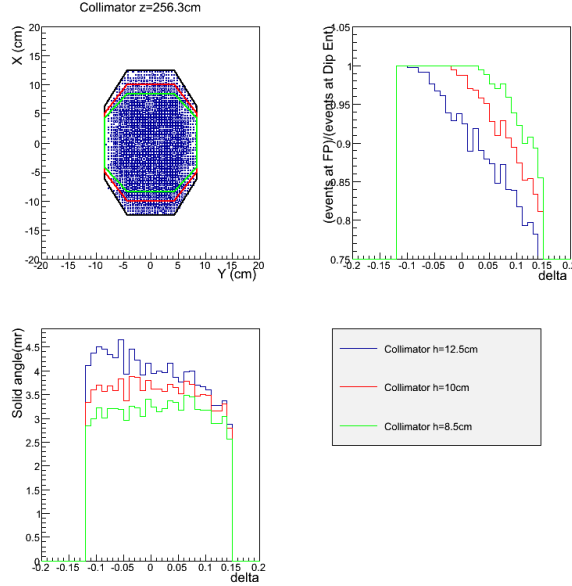


Figure 14: The upper left figure is distribution of events at the location of the collimator with three different vertical size collimators. The lower left figure is the acceptance as a function of  $\delta$  for each of the collimators. The upper right figure is the fraction of events lost in the dipole bore after the dipole entrance.

424 The determination of  $x_{tar}$  independent coefficients 445  
 425 (when  $m = 0$  in Eq. 2) in the reconstructed matrix el- 446  
 426 ements was done using data from specific run settings. 447  
 427 In all cases, a single or multi-foil carbon target is used 448  
 428 with a sieve installed downstream from the target. For 449  
 429 each interaction that pass through a sieve hole, all true 450  
 430 target quantities, including  $x_{tar}$ , can be calculated from 451  
 431 knowledge of the beam position, foil location and sieve 452  
 432 hole location.

433 The calibration of the  $\delta$  matrix elements was done us- 454  
 434 ing carbon elastic data. Using the first order optics from 455  
 435 COSY and selecting events from a carbon target inter- 456  
 436 action that pass through a single hole in the sieve, the 457  
 437 carbon elastic peak and excitation spectrum is clearly 458  
 438 seen as shown in Fig. 16.

439 The carbon energy spectrum shows the elastic peak 460  
 440 and the 4.4 MeV carbon excited state. Additional car- 461  
 441 bon states are observable in the smaller peaks to the 462  
 442 right of the 4.4 MeV peak. The  $\delta$  matrix elements were 463  
 443 optimized by taking a series of runs where the carbon 464  
 444 elastic peak moved across the focal plane for incremen- 465

tal settings of the spectrometer central momentum.

The optimization of the reconstructed target quanti-  
 ties  $y_{tar}$ ,  $y'_{tar}$ , and  $x'_{tar}$  used data from multi-foil carbon  
 targets with the sieve inserted in the beam line. Each  
 hole in the sieve is used to define the true physical values  
 of an event and is compared to the reconstructed angles  
 and positions for optimization. The reconstructed  $y_{tar}$   
 is approximately  $z_{tar} \sin \theta$  where  $\theta$  is the central angle  
 of the spectrometer, and  $z_{tar}$  is the target foil position  
 in the hall beam line coordinate system. To optimize over  
 the full range of possible  $y_{tar}$  values, data must be taken  
 with the spectrometer at various central angles. Two  
 sieves were used to collect the data having the same hole  
 patterns: one where the central hole was centered on the  
 spectrometer axis and the other where the central hole  
 was shifted by half the distance between the holes rela-  
 tive to the spectrometer axis. Data was taken with each  
 sieve separately in order optimize the full spectrometer  
 acceptance. A reconstructed sieve pattern using a single  
 carbon foil is shown in Fig. 17.

The general procedure for the optimization of the

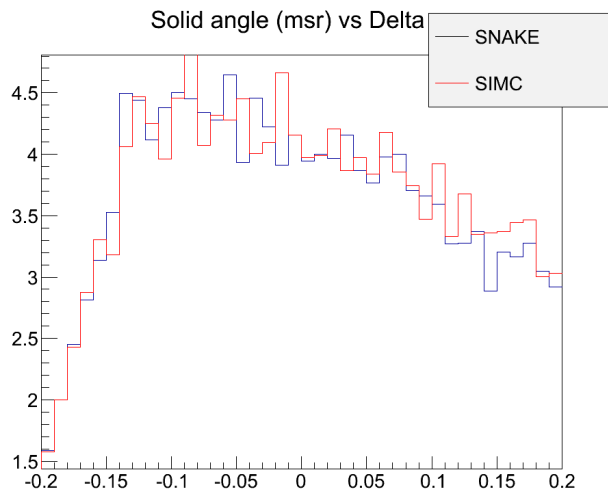


Figure 15: Comparison of predicted SHMS acceptance using the Hall C Monte Carlo (SIMC) and the magnetic transport code SNAKE.

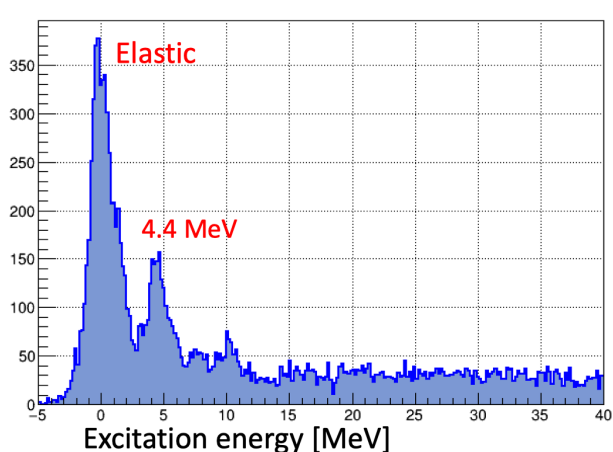


Figure 16: The carbon elastic energy spectrum for events for a single sieve hole, as calculated in terms of delta from the first order optics, clearly shows the carbon elastic peak and the 4.4 MeV excited state.

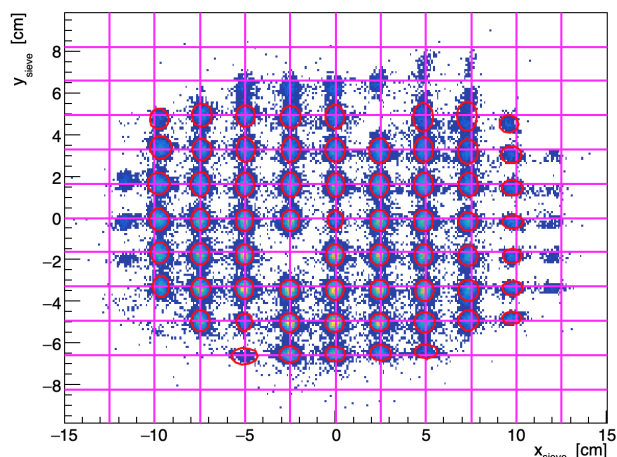


Figure 17: The sieve pattern is reconstructed here where the true sieve hole positions are indicated by the magenta cross lines and the reconstructed holes are outlined in red. The holes at the edges of the sieve are somewhat shifted from the true desired values.

466 target quantities  $y_{target}$ ,  $y'_{target}$ , and  $x'_{target}$  is as follows:  
 467 the events are initially reconstructed using the original  
 468 reconstruction matrix elements generated from the  
 469 COSY model. These events are used to determine the  
 470 true physical values by determining which target foil an  
 471 event originated from and which sieve hole the event  
 472 passed through. The differences between the measured  
 473 events and the real true physical values are minimized  
 474 by solving a Singular Value Decomposition (SVD) to  
 475 calculate the optimized/improved reconstruction matrix

476 elements.

477 Need to mention the reconstructed angular resolutions.  
 478 From CT, I obtained 0.9 mrad horizontal and  
 479 1.1 mrad vertical.

### 480 3.2. Shield House Layout, Shielding Design

481 The radiation environment is an important considera-  
 482 tion for the design of the SHMS shield house, in partic-

ular, the effect of radiation-induced effects on the performance and reliability of detectors and electronics. It has been shown that many new commercial off the shelf components are more sensitive to radiation damage and single event upsets, requiring a careful evaluation of the impact of the radiation-induced effects on their performance and reliability [28, 29]. A specialized SHMS shield house design was thus developed at Jefferson Lab. Shielding thicknesses were optimized using a Monte Carlo simulation and benchmarked against the HMS shielding house, which has proven to provide the necessary detector shielding over more than a decade of experiments at the 6 GeV JLab. A full description of the shielding optimization can be found in Ref. [27].

The primary particle radiation is created when the CEBAF electron beam strikes the experimental target. The main components are scattered electrons, neutral particles (photons and neutrons), and charged hadrons. The energy spectrum of this radiation depends on the incident beam energy and decreases generally as  $1/E$ . It has been shown that the most efficient way to protect the experimental equipment from radiation damage is to build an enclosure around it using certain key materials. The type and thickness of the shield house walls depends on the energy and particle one needs to shield against. However, one may qualitatively expect that the largest amount of shielding material is needed on the side facing the primary source, which in the case of the Hall C focusing spectrometers is the front face. Additional sources of radiation are the beampipe, which extends from the experimental target to the beam dump, and the beam dump area itself. Thus, the faces of the spectrometer exposed to direct sources of radiation are the front, beam side, and the back walls.

Primary and scattered electrons lose a significant amount of energy as they traverse a material by producing a large number of lower energy photons through bremsstrahlung [30]. It is thus important to consider shielding materials that efficiently stop the latter as well.

Neutral particles have a higher penetration power than charged particles. They are attenuated in intensity as they traverse matter, but do not continuously lose energy. Photons interact in materials almost exclusively with electrons surrounding the atom or by pair production in the field of the nucleus. The probability for an interaction depends on the atomic number of the material. Neutrons interact with atomic nuclei in a more complicated way.

An additional source of radiation is due to charged hadrons (e.g. protons, pions). However, the probability for producing hadron radiation is relatively low, and thus will be neglected here. The shielding is, neverthe-

less, effective for charged hadrons. The front wall will, for instance, stop 1 GeV protons.

Fig. 18 shows a schematic of the SHMS shielding plan. The SHMS shield house is similar to the HMS design, but has several new features due to additional requirements. For example, the space between the beam side shield wall and the beam pipe is limited at very forward angles, and in addition, the length of the SHMS detector stack and minimum distance between the back of the detector house to the hall wall requires a reduction in thickness of the concrete shield wall.

Typical beam-target geometries were simulated using Monte Carlo techniques. Simulations were performed using the GEANT MCWORKS distribution, which includes detailed physical and geometric descriptions of the experimental hall and simulates the physics processes using standard GEANT3 together with the DINREG nuclear fragmentation package. Hadronic interactions are treated using the DINREG package, which calculates the probability of such interactions using a database of photonuclear cross sections. For electron-nucleus interactions an “equivalent photon” representation of the electron (or positron) is used.

In this simulation, the CEBAF beam electrons start 1 m upstream of the target, strike it head-on along the cylindrical symmetry axis, and have no momentum component transverse to the beamline. The simulation also includes the beam pipe, target entrance and exit windows, and the entire geometry of Hall C, including all elements of the beam dump. The transmission of particles through the shielding materials was calculated as a function of the material thickness and the angle relative to the beam direction.

A limitation of the radiation studies is the lack of cross section data for low-energy neutrons. The accuracy of the GEANT simulations was tested by benchmark calculations using the MCNP code [31] with an isotropic neutron point source of 1 MeV located 1 m from the shield wall. The MCNP calculations suggest that 50 cm of concrete thermalizes most of the fast neutrons, and after 1 m practically no epithermal neutrons remain. The thermalized neutrons can be captured by a 1 cm Boron layer. In reality, however, the neutron spectrum also includes higher energy neutrons, for instance produced by electrons interacting in the concrete, and thus the actual amount of material for the walls exposed to the primary sources of radiation has to be thicker. A simple transmission calculation using GEANT4 for incident neutron beams of energies between 1 and 10 MeV suggests that a thickness 150 cm of concrete is sufficient to stop the majority of low-energy neutrons [32].

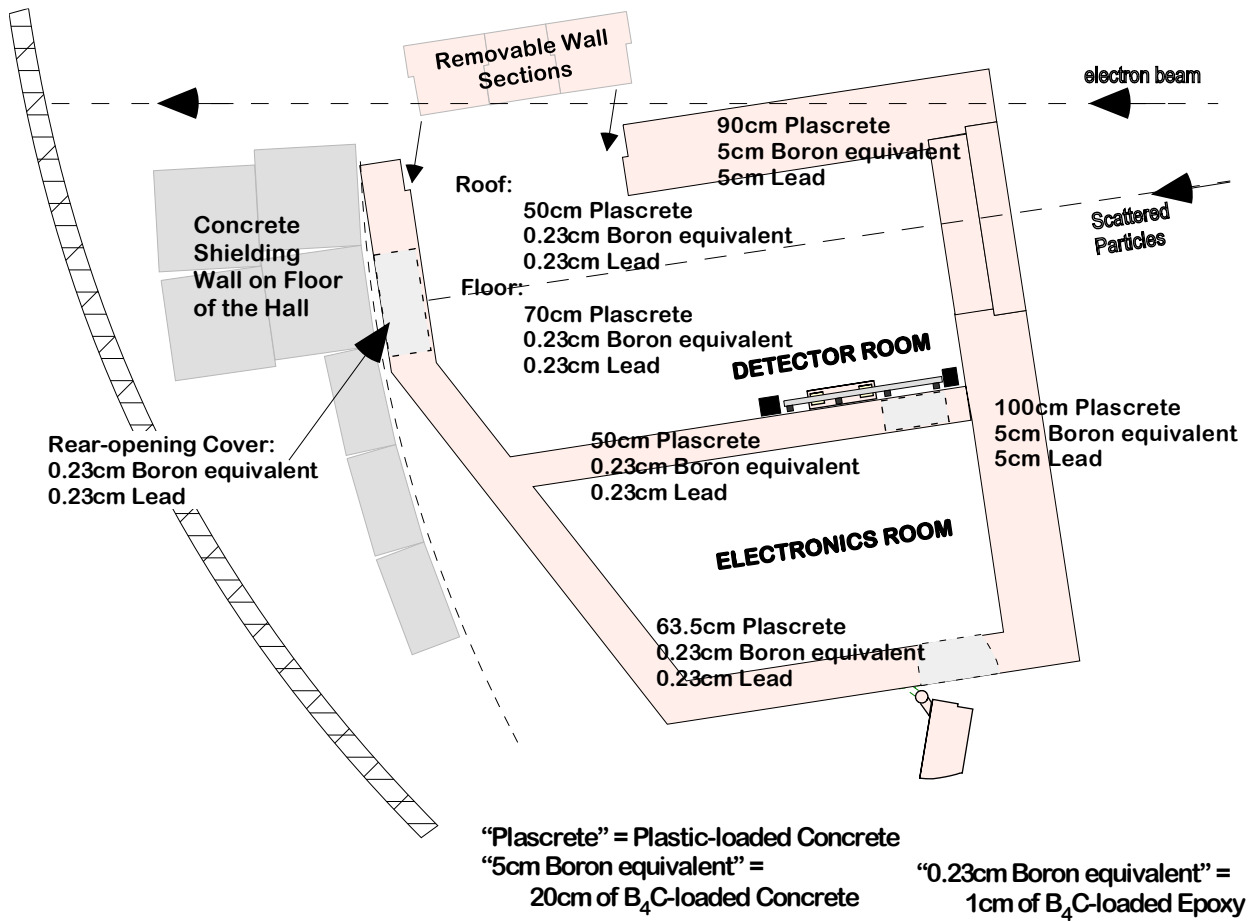


Figure 18: Plan View of the SHMS Shield House showing the layout, thickness, and composition of the walls.

587 The SHMS shielding model is composed of standard 588 concrete ( $\rho=2.4 \text{ g/cm}^{-3}$ ). The thickness of the wall in 589 front of the detector and electronics rooms is 200 cm 590 to shield from the primary radiation source around the 591 target. Figure 19 shows the surviving background flux 592 for varying front wall concrete thicknesses. The results 593 are normalized to the background flux in the HMS at 594  $20^\circ$ . This angle was chosen as experiments in Hall C 595 have shown that electronics problems seem to dominate 596 at lower angles [33]. The simulation results suggest that 597 200 cm of concrete reduces the total flux to half of the 598 HMS at  $20^\circ$ .

599 Figure 20 shows the energy spectra for surviving photons 600 and neutrons with varying front wall thickness. In 601 order to optimize the shielding, these secondary particles 602 have to be absorbed as well. Our assumption on radiation 603 damage is that photons below 100 keV will not be a significant 604 source of dislocations in the lattice of the electronics 605 components, while neutrons will cause radi-

606 ation damage down to thermal energies. Adding lead to 607 the concrete wall reduces the photon flux significantly, 608 but it does not help for neutrons. On the other hand, 609 the boron reduces the flux of very low energy neutrons. 610 Assuming that low energy photons and neutrons cause a 611 significant fraction of the radiation damage, then adding 612 the relevant material would be important.

613 The thickness of the beam-side wall (shielding from 614 an extended source, the beamline) is constrained by the 615 clearance with the detector stack inside the enclosure 616 and the beamline at small angles. Conservatively assuming 617 a clearance of 5 cm between detector stack and the shield 618 wall, the total concrete wall thickness is limited to 105 cm. 619 A 90 cm concrete wall combined with a 5 cm boron and 5 cm 620 lead layer provides the optimal shielding configuration. Adding 621 boron is not much different from adding (or replacing) concrete, 622 but in addition it captures thermal neutrons. 623

624 The majority of charged particles is stopped by the

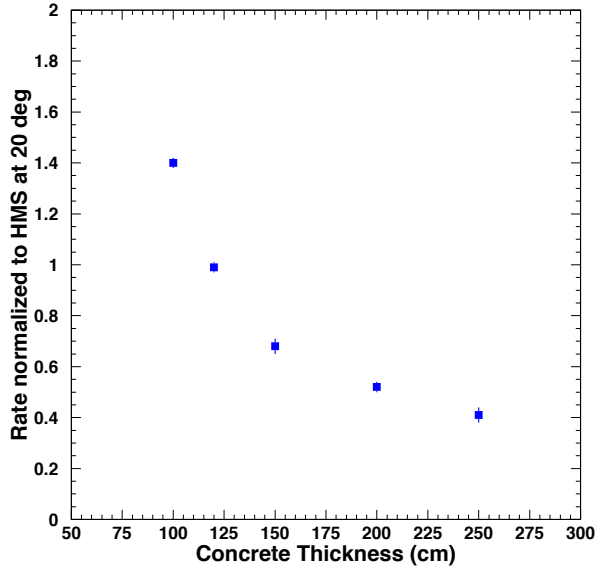


Figure 19: The normalized background rate vs. front wall thickness. The rates are normalized to those found in the HMS at 20°.

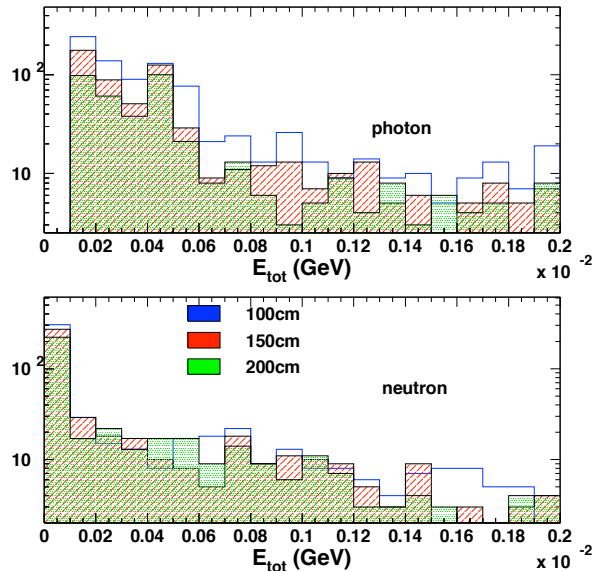


Figure 20: The outgoing particle spectrum, which is soft (< 10 MeV).

625 outer walls of the spectrometer shield house. An addi-  
 626 tional source of radiation may be created from particles  
 627 entering the enclosure through the magnets. In order to  
 628 protect the electronics further, an intermediate wall was  
 629 installed between the detector and electronics rooms.  
 630 Figure 21 shows the normalized rate as the thickness of  
 631 this intermediate wall is varied. This suggests that the  
 632 optimal configuration is provided by a concrete thick-  
 633 ness of 80–100 cm <sup>2</sup>. Further details on shielding con-  
 634 figurations investigated and their optimization can be  
 635 found in Ref. [27].

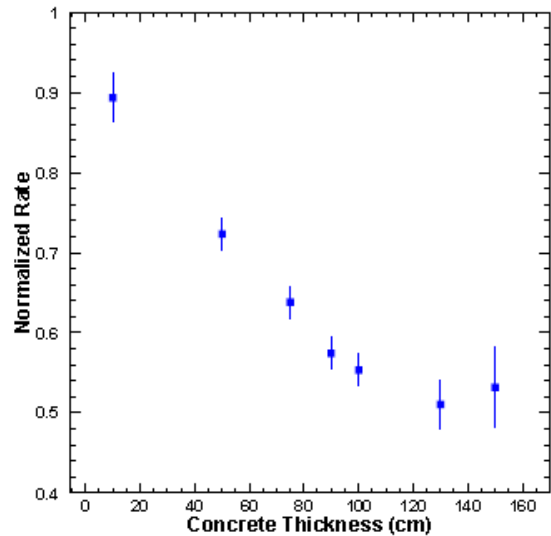


Figure 21: The normalized rate versus the intermediate concrete wall thickness.

636 The hydrogen-rich concrete walls function as a  
 637 shield, an absorber, and a neutron moderator, and are  
 638 thus placed on the outside of all faces of the shield  
 639 house. On the other hand, the ordering of lead and boron  
 640 to shield against the photon and neutron flux may, at first  
 641 glance, not be obvious, and is discussed in detail below.

642 The incoming photon flux has two components: ex-  
 643 ternally produced photons and bremsstrahlung photons  
 644 produced by electrons in the twenty radiation lengths of  
 645 concrete. The simulations have shown that the outgoing  
 646 photon spectrum is soft (<10 MeV). Placing a lead layer  
 647 after the concrete is essential to suppress this low energy  
 648 photon flux. The  $(\gamma, n)$  reaction in lead is not a problem.  
 649 The threshold for the reaction is given by the neutron  
 650 binding energy ( $\sim 8$  MeV). At higher energies, the cross

<sup>2</sup>Note that a minimum wall thickness of 50 cm is needed to provide support for the roof of the shield house

651 sections are in the mbarn range [34]. Even disregarding  
 652 the low cross section, however, it is not clear that this  
 653 reaction adds to the radiating of the electronics, because  
 654 a high energy photon is replaced by a low energy (but  
 655 not thermal) neutron.

656 The incoming neutron flux also has two components.  
 657 Neutrons from excited nuclei will typically not exceed  
 658 10 MeV. The other neutrons are produced through direct  
 659 interactions with only one nucleon in the nucleus.  
 660 These will have high energies, but the flux is low. As  
 661 shown by the MCNP calculation, which has reliable low  
 662 energy neutron cross sections, 0.5 m of concrete almost  
 663 fully thermalizes 1 MeV neutrons. Thus, 2 m of concrete  
 664 should be sufficient to thermalize the first component.  
 665 Some of these will be captured in the concrete, but to  
 666 eliminate the surviving thermal neutrons a layer of boron  
 667 is needed. There are two relevant reaction channels:  
 668  $(n, \gamma)$  and  $(n, \alpha\gamma)$ . The former produces  
 669 high energy photons, but the cross section is relatively  
 670 small. The latter produces a 0.48 MeV photon for every  
 671 captured neutron. The thermal cross section is about  
 672 10 kbarn, and even at 1 MeV it is still in the barn range.  
 673 The majority of neutrons can thus be expected to be  
 674 captured in a sufficiently thick boron layer. An optimal  
 675 shielding configuration would also stop these photons  
 676 produced in the capture. At 0.48 MeV, the photoelectric  
 677 effect and Compton scattering contribute about equally  
 678 to the attenuation in lead. Photons from the latter will  
 679 also need to be absorbed.

680 Thus, placing the lead in front of the boron layer has  
 681 limited benefit. It will not affect the neutron flux, but  
 682 will create an additional source of photons. The more  
 683 lead one places after the boron, the more efficiently  
 684 these photons will be suppressed. From the point of  
 685 view of stopping bremsstrahlung photons, the order of  
 686 boron and lead layers does not matter. Thus, all lead  
 687 should be placed after the boron.

688 Fig. 22 is a photograph showing the resulting multi-  
 689 layered shielding in one of the SHMS shield house  
 690 walls. The ceiling, floor, and other walls have similar  
 691 compositions but varying dimensions as shown in  
 692 Fig. 18. Details about the development of custom  
 693 concrete material containing boron can be found in  
 694 Ref. [35].

695 In summary, the SHMS shielding consists of concrete  
 696 walls to moderate and attenuate particles. Low energy  
 697 (thermal) neutrons are absorbed in a boron layer inside  
 698 the concrete. Low energy and 0.5 MeV capture photons  
 699 are absorbed in lead. With this design, the rates at  
 700 forward angles of  $5.5^\circ$  are estimated to be less than 70%  
 701 of the design goal (HMS at  $20^\circ$ ) in the detector room and  
 702 below 50% in the electronics room.

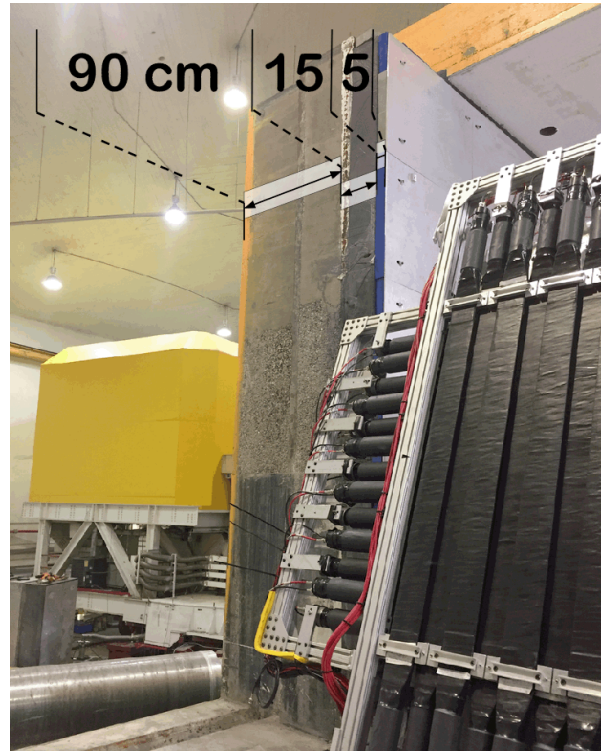


Figure 22: Photograph of the SHMS beam-side shield wall in cross-section view, showing the layers of different materials making up the wall.

### 703 3.3. Scintillator Trigger Hodoscopes

704 The SHMS hodoscope system provides a clean trigger  
 705 and trigger time information as well as the defini-  
 706 tion of the detector package fiducial area, required  
 707 for physics cross section measurements. The system is  
 708 composed of four separate planes of detector paddles:  
 709 S1X and S1Y located immediately after the second drift  
 710 chamber and S2X and S2Y approximately 2.6 m away  
 711 along the z direction. The S1X, S1Y, and S2X planes  
 712 were built using thin scintillator paddles while S2Y uses  
 713 quartz bars.

#### 714 3.3.1. Design and Construction

715 The overall dimensions and granularity of the three  
 716 scintillator planes were driven by the Monte Carlo sim-  
 717 ulations of the SHMS acceptance. The S1X and S1Y  
 718 planes cover a  $1000 \times 980 \text{ mm}^2$  area while the S2X plane  
 719 covers  $1100 \times 1335 \text{ mm}^2$ . Further design constraints  
 720 for this detector include high ( $\geq 99\%$ ) detection effi-  
 721 ciency, position independent along the scintillator pad-  
 722 dle; good time resolution ( $\sim 100 \text{ ps}$ ); high rate capabil-  
 723 ity ( $\sim 1 \text{ MHz/cm}$ ). As the detector's lifetime is assumed

724 to be a decade or more stable, cost effective, and readily  
 725 available materials and readout chain were used.

726 To meet the requirements listed above the SHMS Hodoscope  
 727 was built as a series of arrays (planes) of plastic  
 728 scintillator paddles. The S1X and S1Y planes have 13  
 729 1000x80 mm paddles each, while the S2X plane has 14  
 730 1100x100 mm paddles. For each of the three scintillator  
 731 planes the paddles were staggered by 7 mm and overlapped  
 732 by 5 mm. To minimize the impact of the scintillators  
 733 on downstream detectors and also to ensure good  
 734 timing resolution the thickness of paddles was 5 mm.

735 The scintillator material used was Rexon RP-408.  
 736 The paddles were wrapped by the manufacturer with  
 737 millipore paper, aluminum foil, and 2" wide electrical  
 738 tape. The transition between the thin scintillator material  
 739 and the photomultiplier (PMT) tubes used for readout  
 740 was done using a Lucite fishtail-shaped light guide.  
 741 As the glued joint between the scintillator paddle and  
 742 the light guide is rather fragile (5x80 and 5x100 mm  
 743 joints) aluminum "splints" were used to reinforce it.  
 744 The PMT to fishtail joint was originally wrapped with  
 745 2" tape as well and light-leak tested; subsequently this  
 746 wrapping was reinforced with TEFLON tape and a 3"  
 747 heat-shrink sleeve.

748 Each scintillator is read at both ends by PMTs glued  
 749 to the fishtail using optical glue (BC-600) matching the  
 750 index of refraction of the Lucite. A combination of Photonis  
 751 XP 2262 and ET 9214B 2" tubes were used. Both models  
 752 have 12-stage amplification and their maximum  
 753 photocathode sensitivity is in the blue-green range. The  
 754 typical gain is  $3 \times 10^7$ . Gains were measured as a  
 755 function of high voltage during the construction and  
 756 the whole hodoscope was gain matched *in situ* once  
 757 installed in SHMS.

### 758 3.3.2. Performance

759 All scintillator paddles and the PMTs used to build  
 760 the S1X, S1Y, and S2X planes were extensively tested  
 761 during assembly: the dark current and the gain as a  
 762 function of the high voltage were measured for each  
 763 tube; the finished paddles were light-leak tested and  
 764 their detection efficiency as a function of position along  
 765 the paddle was measured using cosmic rays on an automated  
 766 test stand. A typical gain versus HV graph is shown in  
 767 Fig. 23.

768 Once installed in the SHMS detector hut all paddles  
 769 were retested and gain matched. During the Hall C  
 770 commissioning experiments carried out during the Spring  
 771 2018 the scintillators performed as expected with no  
 772 major problems. [Might want to put more text/a picture  
 773 here, maybe time resolution, efficiency, etc?](#)

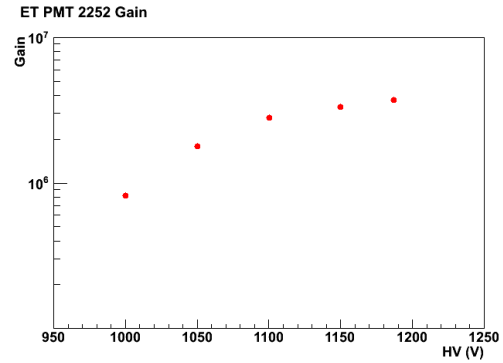


Figure 23: Gain versus high voltage graph for an ET tube used for the scintillator hodoscope.

### 774 3.4. Quartz-bar Trigger Hodoscope

775 The SHMS hodoscope quartz plane was designed to  
 776 help with neutral background rejection in the 12 GeV  
 777 high-rate environment. It operates on the principle of  
 778 Cherenkov light production by electrically charged particles.  
 779 It is one of the four hodoscope planes that form  
 780 the basic 3 out of 4 trigger in the SHMS. In what follows  
 781 the design and construction of this detector will be  
 782 presented as well as its performance with electron beam  
 783 in Hall C.

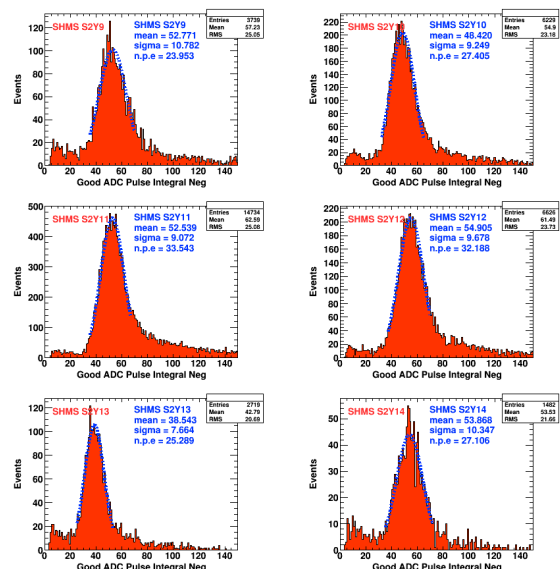


Figure 24: Number of photoelectrons response from the quartz plane.

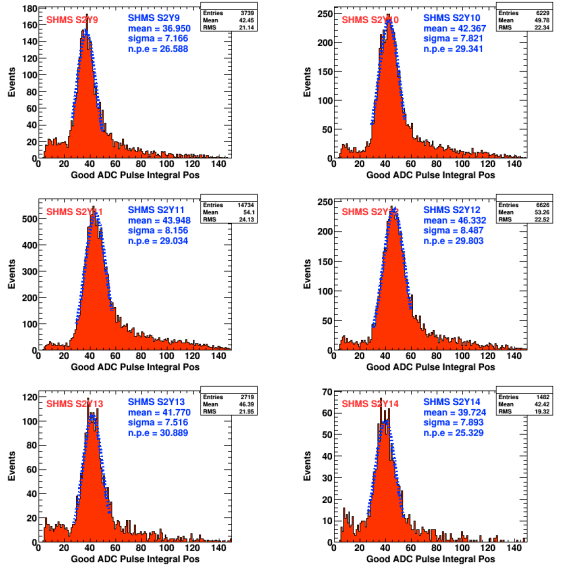


Figure 25: Number of photoelectrons response from the quartz plane.

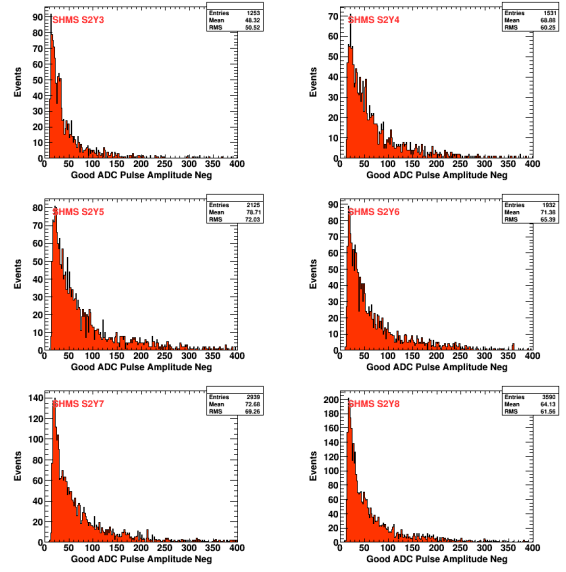


Figure 27: PMT pulse amplitude from protons with momenta of 1.96 GeV.

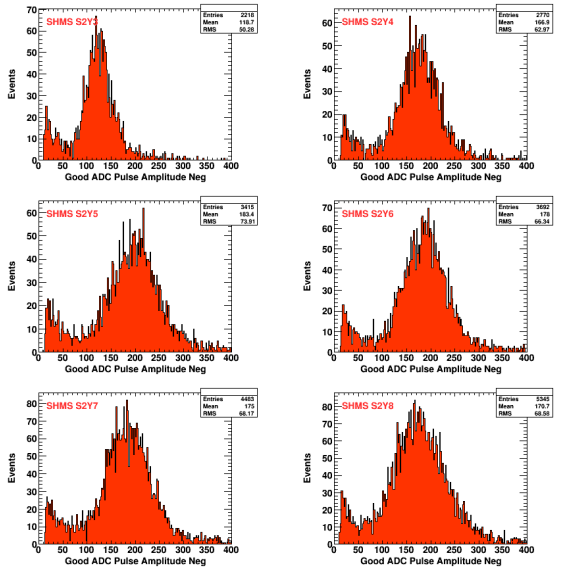


Figure 26: PMT pulse amplitude from pions with momenta of 1.96 GeV.

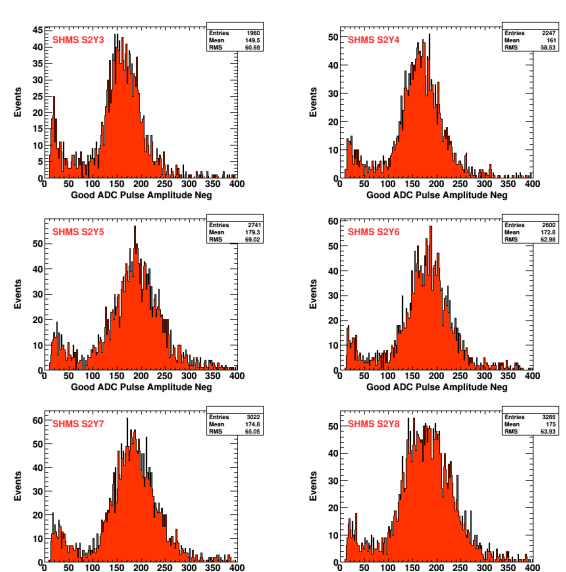


Figure 28: PMT pulse amplitude from protons with momenta of 5.05 GeV.

### 3.4.1. Design and Construction

The design and construction of the SHMS hodoscope quartz plane was done by the North Carolina A&T group led by Abdellah Ahmidouch and Samuel Danagoulian. Quartz bars of  $2.5 \times 5.5 \times 125$  cm<sup>3</sup> dimensions with an index of refraction of 1.5 were chosen. The Cherenkov light produced by electrically charged particles is detected by UV-glass window PMTs (model

ET9814WB) quartz window ET9814QB photomultiplier tubes optically coupled to the quartz bars through RTV615 silicon rubber of  $50 \mu$  thickness. There are 16 bars in use in the hodoscope quartz plane are staggered so that there is an overlap between adjacent bars of 0.5 cm. The quartz plane frame allows for more bars to be added.

### 3.4.2. Performance

The performance of the detector was studied with beam during the Hall C commissioning in Fall of 2017. A plot of the photoelectron response from most bars in the quartz plane is shown in Fig. 24 and Fig. 25. Only electrons with an incident angle close to 90 deg were chosen here to eliminate the bias coming from possibly reduced photon collection efficiency due to sub-optimal angles of the photon cones. All PMTs and optical couplings performed satisfactory.

The threshold for Cherenkov light production in the quartz bars for electrons, pions, kaons and protons is shown in Fig. TBD. Beam data confirmed the expectation that the detection efficiency for low momentum protons, for example, will be smaller than that for pions or electrons simply due to the reduced number of Cherenkov photons that particles close to their firing threshold will produce. This is exemplified by Fig. 26, Fig. 27 and Fig. 28.

### 3.5. Drift Chambers

The SHMS horizontal drift chambers provide information to determine the trajectory of charged particles passing through the detector stack. The drift chamber package consists of two horizontal drift chambers separated by a distance of 1.1 m and oriented in the detector stack such that the sense wires planes are perpendicular to the central ray. Each chamber consists of a stack of six wire planes providing information on the track position along a single dimension in the plane of the wires and perpendicular to the wire orientations to better than  $250 \mu\text{m}$ . The perpendicular distance of the track relative to the wire is determined from the time of the signal produced by the ionization electrons as they drift from their production point to the wire in an electric field of approximately 3700 V/cm.

The basic design and construction technique is based on that of previous successful chambers built for the Hall C 6 GeV program, which have been shown to reach the resolutions and particle rate specifications of the SHMS. The open layout design consists of a stack of alternating wire and cathode foil planes; each plane consisting of 1/8 inch thick printed circuit board (PCB). These are sandwiched between a pair of aluminum plates on the outside, which provide both the overall structural support and the precise alignment of each board via dowel pins at the corners. Just inside each plates is a fiberglass board with the central area cut out and covered with a vacuum stretched film of aluminumized Mylar, which provides the gas window. These are sealed to prevent gas leakage via an o-ring around the gas fitting through-hole on the inside of the plate.

Each chamber consists of two identical half chambers separated by a fiberglass mid-plane, which also supports the amplifier discriminator cards required for the sense wire readout. To minimize the production costs, only two unique PCB types were designed: an X-plane with wires oriented horizontally (left panel of Figure 29), and a U-plane with wires oriented at  $+60^\circ$  relative the X-plane (right panel of Figure 29). All other plane orientations are generated by rotations of these two basic board types. For instance, the boards are designed such that a rotation of 180 in-plane about an axis through the center of the board produces boards with wires of the same orientation, but shifted by 1/2 cell width, thus allowing the resolution of left/right ambiguities. Rotation of Figure 29 such that the top becomes the bottom produces the X' and U' orientations. The V and V' boards with wire orientation of  $-60^\circ$  relative to the X-plane are produced by a rotation of the U and U' boards of  $180^\circ$  into the page about a vertical axis through the center of the board. Each half chamber has three planes with the first half consisting of (U, U', X) and the second half consisting of (X', V', V). The first chamber is oriented in the SHMS frame such that the board ordering as seen by particle traversing the spectrometer is (U, U', X, X', V', V), while for the second chamber the ordering is reversed (V, V', X', X, U', U). A drawing showing the chambers mounted in the frame is presented in Figure 30.

The drift gas (50/50 mixture of Ethane/Argon in production mode) flows across each board through holes in the cathode planes (k-planes) alternating from top to bottom. A technical drawing of a k-plane is presented in Figure 29. The overall dimensions of the wire chambers are driven by the desired active area for particles at the focal plane of the SHMS; this has been set at 80 cm x 80 cm. The active area of each wire plane consists of alternating  $20 \mu\text{m}$  diameter gold tungsten sense wires and  $80 \mu\text{m}$  diameter copper plated beryllium field wires separated by 0.5 cm. Each wire plane is sandwiched between a pair of cathode planes with the cathode surfaces consisting of 5 mil thick stretched foils of copper plated Kapton.

## 3.6. Heavy-Gas Cherenkov Counter

### 3.6.1. Design

The SHMS Heavy-Gas Cherenkov detector (HGC) is a threshold-type Cherenkov detector, designed to separate charged  $\pi$  and  $K$  over most of the SHMS operating momentum range, 3–11 GeV/c.  $\text{C}_4\text{F}_{10}$  radiator gas at 1 atm, with an index of refraction of  $n=1.00143$  at standard temperature [14], allow  $\pi^\pm$  to produce abundant

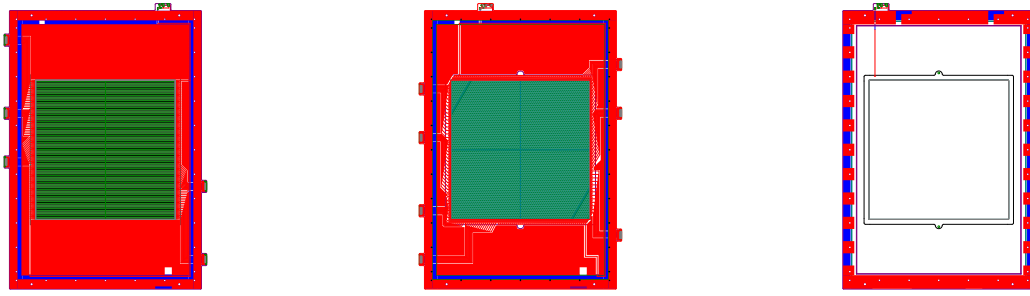


Figure 29: Technical drawings of the PCBs for the X-plane (Left), U-plane (Middle), and K-plan (Right).

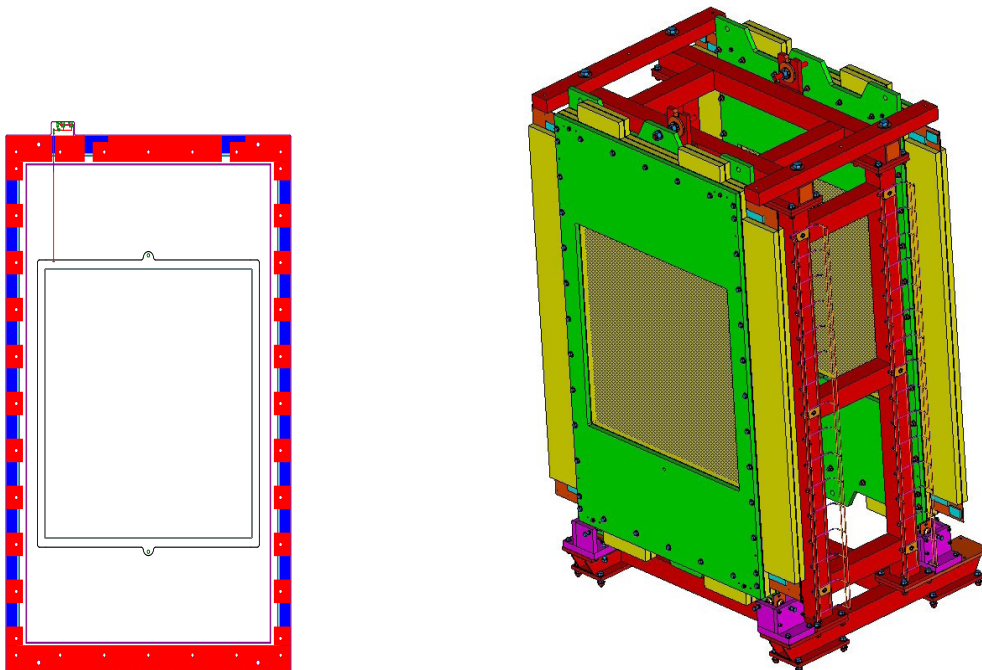


Figure 30: (Left) Technical drawing of cathode (k-plane) PCB. (Right) Technical drawing of the two drift chambers mounted in the Aluminum frame such that the scattered particles would enter the chamber from the left. The chambers are fixed to the frame by a bolt through the top tab on the chamber plate which allows for fine adjustments to the pitch. The downstream chamber (DC2) is mounted in the reverse orientation from the upstream chamber (DC1).

900 Cherenkov light above 3 GeV/c momentum, while  $K^\pm$  911  
 901 remain below Cherenkov threshold until about 7 GeV/c. 912  
 902 Optimal  $\pi/K$  separation at higher momenta require 913  
 903 a reduction in the gas pressure, down to 0.3 atm at 914  
 904 11 GeV/c. 915

905 A schematic view of the detector is shown in Fig. 31. 916  
 906 The SHMS focal plane is subtended by four 55×60 cm 917  
 907 0.3 cm thick glass mirrors, which reflect the Cherenkov 918  
 908 radiation to four Hamamatsu R1584 12.5 cm diameter 919  
 909 photomultiplier tubes located above and below the par- 920  
 910 ticle envelope. The mirrors and gas are enclosed in a 921

911 cylindrical aluminum tank of 164.9 cm inner diameter 912  
 and 113.5 cm length, with entrance and exit windows of 913  
 0.102 cm thickness 2024 T-4 aluminum alloy [15]. The 914  
 vessel is sufficiently strong to be pumped to vacuum be- 915  
 fore introducing the radiator gas, avoiding the need to 916  
 purge when filling. A unique aspect of the detector is 917  
 the placement of the photomultipliers outside the gas 918  
 envelope, viewing the enclosure through 1.00 cm thick 919  
 Corning 7980 quartz windows. This allows the gas en- 920  
 closure to be smaller in diameter than otherwise, as the 921  
 full length of the PMT and base no longer had to be

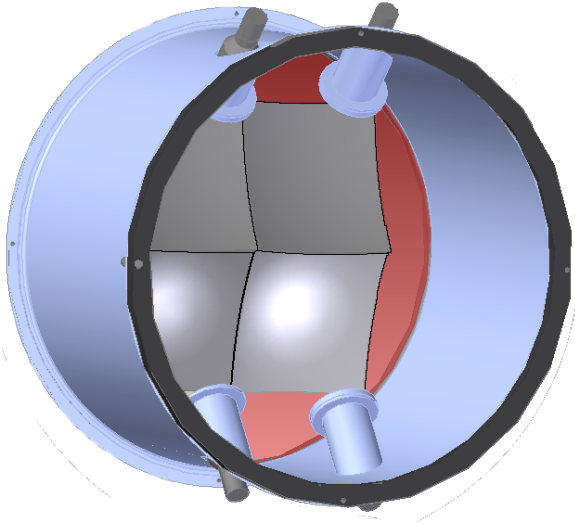


Figure 31: 3D-CAD rendering of the Heavy Gas Cherenkov Detector.

922 fully within the diameter of the vessel. It also makes the  
 923 PMTs available for servicing without venting the gas.

924 The mirrors are inexpensive, having been produced  
 925 by the slumping process [16]. As a result, they deviate  
 926 from the desired 110 cm radius of curvature with  
 927 a slightly oblate shape [17]. However, the Cherenkov  
 928 cone on the mirrors for 3-7 GeV/c  $\pi^\pm$  in  $C_4F_{10}$  is 7-  
 929 10 cm in diameter, so optical quality mirrors are not  
 930 required for this application. The UV wavelength char-  
 931 acteristics of the respective optical components are rel-  
 932 atively well matched.  $C_4F_{10}$  has good transmittance  
 933 down to  $\sim 160$  nm [14]. The quartz viewing windows  
 934 provide  $>88\%$  transmission down to 200 nm, including  
 935 the  $\sim 10\%$  loss due to surface reflection [18], and the op-  
 936 tical glass face PMTs have 70% of their peak quantum  
 937 efficiency at 200 nm (peak at 350 nm) [19]. Accord-  
 938 ingly, the mirror reflectivity was optimized for  $>90\%$  at  
 939 270 nm, and 75% at 200 nm [20].

### 940 3.6.2. Calibration

941 The goal of the calibration procedure is to generate  
 942 an accurate translation from raw FADC channels (or  
 943 charge in pC) to the number of photoelectrons emit-  
 944 ted from the cathode surface of the PMT (NPE). This  
 945 is achieved by isolating the single photoelectron (SPE)  
 946 peak, yielding a calibration, and then verified by exam-  
 947 ining the regular spacing of the first few photoelectron  
 948 contributions in the ADC spectrum.

949 To isolate the SPE peak, tracking cuts are applied  
 950 to the data to analyze what each PMT detected from

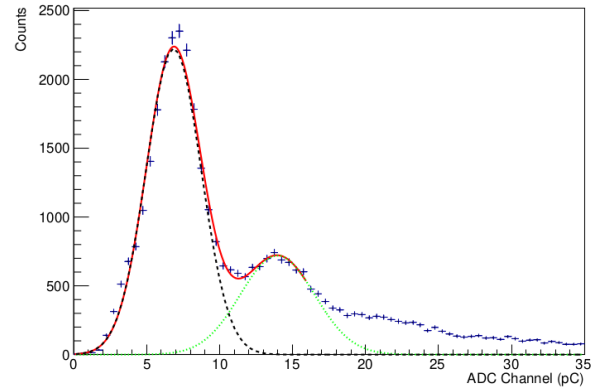


Figure 32: The isolated 1 (dashed black) and 2 (dotted green) photoelectron peaks for the lower right PMT #2, and their sum (solid red), obtained by selecting adjacent mirror light from the upper right quadrant #4. Three such adjacent mirror plots are obtained for each PMT. The light from the mirror closest to the PMT is far more intense, with too few SPE events available to yield a reliable calibration.

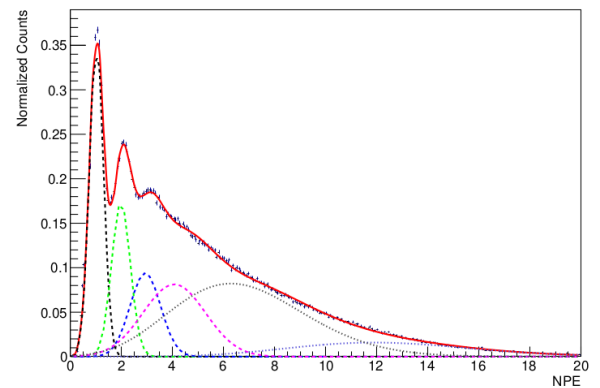


Figure 33: Results from a successful calibration of the HGC. Shown is the NPE distribution of the lower right PMT #2 obtained from all four mirrors. The 1, 2, 3 NPE peaks are shown, indicated by dashed Gaussian distributions. Two Poisson distributions (dotted lines) provide a good description of the nearest mirror events with large NPE, and a broad Gaussian near 4 NPE fills in the gap with the lower NPE peaks. The sum of all 6 distributions is shown as the solid red curve.

951 charged particles traversing each mirror quadrant. As a  
 952 charged particle passes through a mirror quadrant, the  
 953 produced Cherenkov cone allows some light to be inci-  
 954 dent on adjacent mirrors. As each mirror is focused on  
 955 a single PMT, one PMT will receive most of the pro-  
 956 duced light while the other three receive much smaller  
 957 amounts. This small signal allows the SPE peak to be  
 958 measured, yielding a reliable calibration. To select this  
 959 adjacent mirror light, cuts (based on the physical dimen-  
 960 sions of the mirrors) are placed on the tracked coordi-  
 961 nates of the charged particles, extrapolated to the HGC

962 mirror plane,

$$x_{\text{HGC}} = x_{\text{Focal Plane}} + x'_{\text{Focal Plane}} \cdot z_{\text{HGC}} \quad (3)$$

$$y_{\text{HGC}} = y_{\text{Focal Plane}} + y'_{\text{Focal Plane}} \cdot z_{\text{HGC}}, \quad (4)$$

963 where  $z_{\text{HGC}} = 156.27$  cm is the distance from the fo-  
 964 cal plane to the HGC mirror plane. The coordinate axis  
 965 for the HGC is the convention used in charged particle  
 966 transport in dispersive magnetic systems. The  $x$ -axis is  
 967 the direction of increasing particle momentum, the  $z$ -  
 968 axis is the direction of particle travel through the spec-  
 969 trometer, and the  $y$ -axis is deduced from  $z \times x$ . Addi-  
 970 tionally, timing cuts are applied to the HGC data, col-  
 971 lected using the high resolution pulse time setting in the  
 972 FADC250's FPGA. The time measured corresponds to  
 973 the time it takes a pulse to reach half of its maximum  
 974 amplitude after passing a pedestal threshold of 5 mV.  
 975 Lastly, a cut on particle velocity,  $\beta$ , is also applied, ob-  
 976 tained from the tracking algorithm.

977 An example of a completed calibration is shown in  
 978 Figs. 32, 33. For this run, the HGC was filled with  
 979  $\text{C}_4\text{F}_{10}$  at 1 atm, and the SHMS central momentum  
 980 was 2.583 GeV/c, with polarity set to detect positively-  
 981 charged particles. Cherenkov radiation is produced by  
 982  $\pi^+$  traversing the HGC with momentum  $> 2.598$  GeV/c.  
 983 This can occur only for  $\delta > +0.5\%$ , which corresponds  
 984 roughly to the bottom half of the HGC. Subthreshold  $\pi^+$   
 985 with  $\delta < +0.5\%$ , as well as  $K^+$  and  $p$ , may produce low-  
 986 level light in the HGC via knock-on electron emission  
 987 and scintillation in the radiator gas. The adjacent mir-  
 988 ror cuts described above produce a clear SPE peak in  
 989 Fig. 32, which provides the main source of calibration  
 990 information. A histogram of light collected in one PMT  
 991 from all four mirrors is shown in Fig. 33, where the av-  
 992 erage number of photo electrons detected per event is  
 993 higher due to the more intense light from the closest  
 994 mirror. In this figure, the spectrum is fit with a sum of  
 995 four Gaussian and two Poisson distributions, shown by  
 996 the solid red line.

997 An inherent systematic uncertainty is present in the  
 998 HGC calibration due to statistical errors in determining  
 999 the location of the SPE peak in the various mirror quad-  
 1000 rants. This uncertainty was quantified by recording the  
 1001 locations of the SPE across several runs, for the different  
 1002 adjacent mirror combinations for each PMT, as well as  
 1003 by varying the contribution of the higher PE tail extend-  
 1004 ing underneath the SPE peak, as in Figs. 32, 33. The  
 1005 systematic uncertainty in the calibration is taken to be  
 1006 the root mean square of this set of values, giving  $\pm 1.5\%$ .  
 1007 It should be noted this uncertainty is somewhat larger  
 1008 than the statistical uncertainty of the SPE peak, which  
 1009 is typically 0.2 to 0.6%.

### 1010 3.6.3. Gain Matching

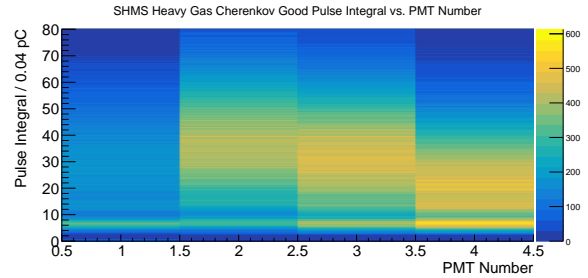


Figure 34: Demonstration of gain matching between PMTs by the alignment of the single photoelectron, indicated by the yellow band about 6.825 pC. The horizontal axis refers to PMT number, the vertical axis to Pulse Integral in bins of 0.04 pC. The color axis represents the number of events filling each bin.

1011 To ensure each PMT has an identical response to in-  
 1012 cident light, the voltages of each PMT were adjusted to  
 1013 obtain accurate gain matching. This can be seen in Fig-  
 1014 ure 34 by the alignment of the SPE at approximately  
 1015 6.825 pC, represented by the common band across all  
 1016 four PMTs at that value. Additionally, the gain of each  
 1017 PMT was tested by the manufacturer, Hamamatsu, and  
 1018 at Jefferson Lab. The results of each test are shown in  
 1019 Table 3. The Hamamatsu data were taken directly at  
 1020 2000 V in a highly controlled environment, thus leading  
 1021 to small uncertainty in the gain which was not quoted.  
 1022 The Jefferson Lab measurement were also taken at 2000  
 1023 V, but taken in an experimental environment. This gives  
 1024 rise to an uncertainty in the JLab gain data on the order  
 1025 of 1%, larger than the Hamamatsu data.

### 1026 3.7. Noble-Gas Cherenkov Counter

#### 1027 3.7.1. Design

1028 Analyzing momenta up to 11 GeV/c at scattering an-  
 1029 gles from 5.5 to 40.0 degrees, the SHMS will reach  
 1030 kinematic regions in which the pion background rate  
 1031 dominates the scattered electron rate by more than  
 1032 1000:1. The suppression of these anticipated pion

PMT	JLab Gain	Hamamatsu Gain
PMT 1	$(2.79 \pm 0.01) \times 10^7$	$0.969 \times 10^7$
PMT 2	$(6.55 \pm 0.04) \times 10^7$	$3.60 \times 10^7$
PMT 3	$(7.12 \pm 0.05) \times 10^7$	$5.79 \times 10^7$
PMT 4	$(5.35 \pm 0.04) \times 10^7$	$3.20 \times 10^7$

Table 3: Gain characteristics for the PMTs in the HGC. Two measurements were performed, one at Jefferson Lab in an experimental setting, and one by the manufacturer Hamamatsu. The set voltage for the gain measurements is 2000 V for each PMT.

1033 backgrounds while maintaining efficient identification  
 1034 of electrons is therefore one of the main duties of the  
 1035 SHMS detector elements and the SHMS Noble Gas  
 1036 Cherenkov Detector shoulders a large portion of this  
 1037 particle identification burden. The design of the noble  
 1038 gas threshold Cherenkov detector is such that it will  
 1039 meet these twin goals of suppression and identification.  
 1040 The main goal of the detector is to distinguish between  
 1041 electrons and pions with momenta between 6 GeV and  
 1042 11 GeV/c. Operating at 1 ATM it will use a mixture  
 1043 of Argon and Neon as the radiator: pure Argon with an  
 1044 index of refraction  $n=1.00028201$  at a SHMS momenta  
 1045 of 6 GeV/c and pure Neon with an index of refraction  
 1046  $n=1.000066102$  at 11 GeV/c and a mixture of Argon  
 1047 and Neon at intermediate momenta.

1048 The SHMS NGC design was restricted by the available  
 1049 space and the need to have good discrimination at the  
 1050 highest momenta. The number of photoelectrons is  
 1051 maximized in this design by the use of quartz window  
 1052 PMTs and mirrors with excellent reflectivity well into  
 1053 the UV.

1054 The NGC consists of the four main elements: 1) a  
 1055 light tight box with thin entrance and exit windows  
 1056 designed to operate at 1 Atm; 2) four spherical mirrors  
 1057 held in a rigid frame; 3) four 5 inch quartz window  
 1058 photomultipliers (PMTs) and 4) the radiator gas.

1059 The tank was fabricated with an internal rigid aluminum  
 1060 t-slot frame and thin aluminum walls welded together  
 1061 and has an active length of 2m along the beam direction  
 1062 and approximately 90 cm perpendicular to the beam  
 1063 direction. The main access is provided through a large  
 1064 'door', and four small panels provide modest access  
 1065 to the PMTs. The tank has feedthroughs for gas  
 1066 management as well as for HV and signal cables. The  
 1067 interior was painted with a black flat paint to prevent  
 1068 the reflection of light from cosmic rays or hall background.  
 1069 Thin entrance and exit window made of two layers of  
 1070 2 mils of the Dupont product Tedlar( $\text{CH}_2\text{CHCl}$ )<sub>n</sub>. The  
 1071 PMTs were positioned outside the active area of the  
 1072 scattered particles, achieved by a 15° tilt of the mirrors.

1073 Four spherical thin glass mirrors of radius 135 cm,  
 1074 square in shape with edges of 43 cm focus the  
 1075 Cherenkov light onto to the PMTs. The glass blanks  
 1076 were manufactured by Rayotek Scientific[24] of San  
 1077 Diego from borosilicate glass of 3 mm thickness by  
 1078 slumping over a polished steel mold and then cut to  
 1079 dimensions. As simulation showed a reduction of  
 1080 collection efficiency due to incoming photons losses at  
 1081 the exposed edges of the mirror were beveled by away  
 1082 from the active surface to minimize scattering from  
 1083 these edges.

1084 The final batch of the glass blanks was shipped to

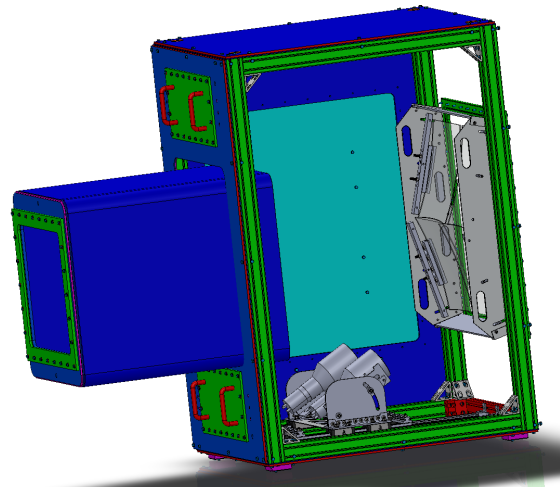


Figure 35: Sketch of the NGC tank. This view is possible as one panel is removed. Note the PMT mounting system is different than shown here.

Apex Metrology Solutions of Fort Wayne for the CMM shape scanning measurements. Apex's measurements were performed on the grid of 1806 points. The data were fitted with spherical, conical and elliptical fit functions for each mirror. Though the elliptical fit described the surface slightly better than the spherical fit the updated simulation with the real measured parameters showed almost no difference in the collection efficiency between the two. In addition the same fitting was performed for 5 selected locations on the mirror: entire mirror, the center, and 4 quadrants. Based on the spherical fit results "best" mirrors and "best" corners for each mirror were identified. The 4 mirrors come together and overlap at the center of the acceptance where a majority of the scattered electrons are focused. Care was then made to select among the best 4 glass pieces their best corners so as to be in the overlap region. The radii of the 4 best pieces of glass, from fitting, was found to never vary by more than 2 cm from the contracted value of 135 cm in fit areas described above.

The blanks were coated by the Thin Film and Glass Service of the Detector Technologies Group at CERN[25]. The reflectivity was also measured at CERN and found to be excellent well into the UV (Fig. 36).

The four mirrors are arranged in a 2 by 2 array with a small overlap in the center, providing full coverage over the active area. In order to accomplish this without mechanical interferences the mirrors were staggered at slightly different along the tank z-axis. The mirrors

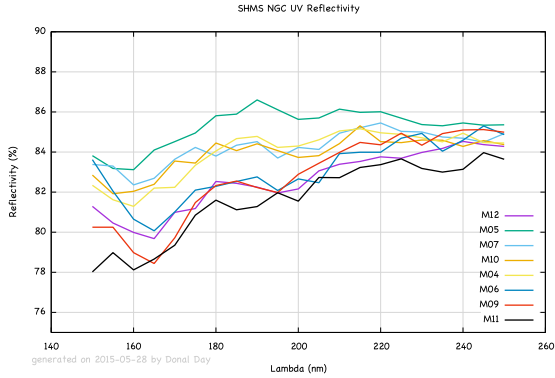


Figure 36: The UV measured reflectivity of the finished mirrors, coated at CERN which is no less than 78% at 150 nm. Between 250 nm and 600 nm the reflectivity rises to almost 90%.

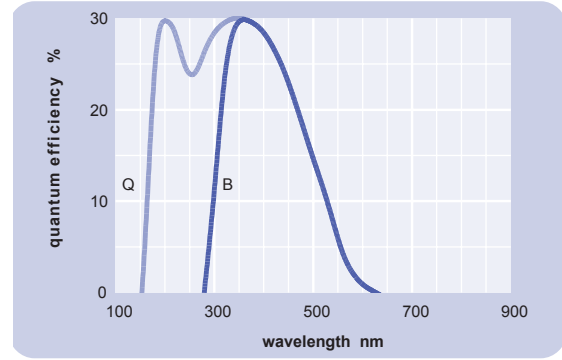


Figure 38: Quantum efficiency of Electron Tubes Enterprises model 9823QKB04 - light blue curve, labeled “Q”.

1115 were mounted in a monolithic frame installed as single  
 1116 unit. See Figure 37, and are tilted at 15° off the z-axis  
 1117 to place the PMTs to be outside the active area.



Figure 37: Frame with mirrors about to be moved into tank.

1118 The four PMTs are 14 stage 5 inch quartz win-  
 1119 dows PMTs manufactured by Electron Tubes Enterprises  
 1120 [26], model 9823QKB04. The tubes are surrounded by  
 1121 a mu-metal shield and the HV is distributed to the stages  
 1122 by a positive base. The 9823QKB04 has a quantum effi-  
 1123 ciency above 5% at 150 nm and 30% at 350 nm as seen  
 1124 in Figure 38.

- 1125 3.7.2. Optics Tuning
- 1126 3.7.3. Calibration
- 1127 3.7.4. Gain Matching
- 1128 3.7.5. Performance
- 1129 3.8. Aerogel Cherenkov Counter
- 1130 3.8.1. General Design Overview

1131 The detector design is summarized in Fig. 39 which  
 1132 shows a photograph of the aerogel counter installed  
 1133 downstream of the cylindrical HGC in the SHMS de-  
 1134 tector stack. The detector consists of two main com-  
 1135 ponents: a tray which holds the aerogel material, and a  
 1136 light diffusion box with photomultiplier tubes (PMTs)  
 1137 for light readout. Four identical trays for aerogel of  
 1138 nominal refractive indices of 1.030, 1.020, 1.015 and  
 1139 1.011 were constructed. The design allows for easy de-  
 1140 tector assembly and replacement of the aerogel trays.  
 1141 Using up to 9 cm aerogel thickness in the trays, the total  
 1142 depth of the detector is 24.5 cm along the optical axis of  
 1143 the SHMS. A detailed discussion of the detector, char-  
 1144 acterization of its components, and performance tests  
 1145 can be found in Refs. [36, 13].

Table 4: Threshold momenta  $P_{Th}$  for Cherenkov radiation for charged muons, pions, kaons, and protons in aerogel of four refractive indices ranging from  $n=1.011$  to 1.030.

Particle	$P_{Th}$ $n=1.030$	$P_{Th}$ $n=1.020$	$P_{Th}$ $n=1.015$	$P_{Th}$ $n=1.011$
$\mu$	0.428	0.526	0.608	0.711
$\pi$	0.565	0.692	0.803	0.935
$K$	2.000	2.453	2.840	3.315
$p$	3.802	4.667	5.379	6.307

1146 The diffusion box is made of the aluminum alloy  
 1147 6061-T6. The side panels are constructed of ~2.5 cm

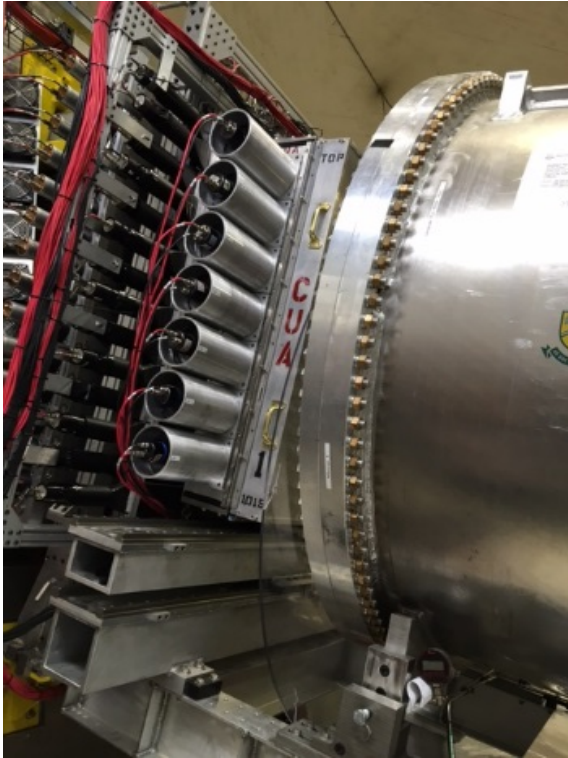


Figure 39: Photograph of the aerogel Cherenkov detector (“CUA” printed on the side of the radiator tray) installed in the SHMS detector stack. To its right is the Heavy Gas Cherenkov. On the left can be seen the edge of the s2x and s2y hodoscope arrays.

(1-inch) plates. The back cover is  $\sim 1.6$  mm (1/16 inch) thick. The inner dimensions of the box are  $\sim 103 \times 113 \times 17.3$  cm<sup>3</sup> (40.5”  $\times$  44.5”  $\times$  6.82”). To optimize light collection the inner surface of the diffusion box is lined with either 3 mm (covering  $\sim 60\%$  of the surface) or 1 mm (remaining  $\sim 40\%$  of the surface) thick GORE reflector material [37]. This material has a reflectivity of about 99% over the entire spectrum.

The light collection is handled by 5-inch diameter photomultiplier tubes (XP4500). The 5.56” (14.1 cm) diameter cylindrical housings holding the PMTs are mounted upon 14 waterjet cut circular openings on the left and right (long) sides of the diffusion box, with minimum spacing of 14.92 cm (5.875”) between the centers. The PMTs are sealed into their housing using a light-tight synthetic rubber material (Momentive RTV103 Black Silicone Sealant) and the whole assembly is sealed light-tight. The mechanical design includes six openings on the top of the diffusion box, presently covered with blanks, that can be used to increase the signal output from the detector by about 30%, if needed.

The magnetic shielding for the PMTs consists of

13.5 cm (5.316”) diameter  $\mu$ -metal cylinders, which were constructed to end abreast with the PMT window. The construction also features bucking coils that can be installed on the PMTs, if excessive residual magnetic fields appear to be present in the SHMS hut.

The aerogel trays are of the same transverse size as the diffusion box but 11.3 cm (4.45”) deep. The front cover of the trays is made of a 5 mm thick honeycomb panel with effective Aluminum thickness to  $\sim 1.3$  mm (0.050”). The inner surface of the SP-30 and SP-20 aerogel trays is covered with 0.45  $\mu$ m thick Millipore paper Membrane GSWP-0010 (Millipore) of reflectivity of about 96% [38]. Though Millipore is difficult to handle, its chemical inertness makes it superior to reflective paints. For the two lower refractive index trays (SP-15 and SP-11), in order to optimize light collection, we used 1 mm thick GORE diffusive reflector material (DRP-1.0-12x30-PSA) with reflectivity of about 99%.

For the Cherenkov radiator high transparency aerogels were used. The higher two of the refractive indices (SP-30 and SP-20) were originally manufactured by Matsushita Electric Works, Ltd. The lower two indices (SP-15 and SP-11) were manufactured by Japanese Fine Ceramics Center. These tiles have dimensions of approximately 11 cm by 11 cm by 1 cm. They feature a waterproof coating that make them hydrophobic [39, 40]. This removes the need for baking (which in fact would destroy the coating). Detailed studies of the aerogel characteristics are presented in Ref. [36].

The trays were filled with aerogel tiles layer by layer. In each layer the tiles were laid down flat and arranged in a brick pattern to minimize holes in the radiator. To fill gaps of less than the size of a full tile at the edges of the tray the aerogel material was cut using a diamond coated saw or razor depending on the refractive index of the material. The aerogel radiator is on average  $\sim 9$  cm thick (8 layers). The SP-30, SP-20 and SP-15 aerogel trays were filled over their entire 110 cm  $\times$  100 cm area. The SP-11 aerogel tray radiator covers only the active area of 90 cm  $\times$  60 cm required by the experiments [41, 42, 60, 43, 59]. An inner frame has been designed to arrange the aerogel tiles inside the active area of this tray. The sides of this inner frame are made of carbon fiber square tubes. This assembly allows future X-Y repositioning of the inner frame inside the tray.

To protect the aerogel radiator from severe damage in case of accidental flipping over of a tray during installation, a net of thin stainless steel wires is installed in close proximity to the aerogel surface. This is a technique previously tested in aerogel detectors at JLab [44]. The wires form an interweaving grid by running between stainless steel screws on the sides of the box.

1222 Small springs attached to the ends of wires provide nec- 1268  
1223 essary tension.

1224 An aerogel tray attaches to the diffusion box by 1269  
1225 means of bolting through flanges surrounding both 1270  
1226 boxes. A round O-ring running in a shallow groove 1271  
1227 along the diffusion box sides ensures a light tight con- 1272  
1228 nection. The entire detector is designed so that it can be 1273  
1229 removed from the sliding detector stand that positions 1274  
1230 the detector into the SHMS detector stack. 1275

### 1231 3.8.2. Performance aspects 1276

1232 The light collection performance of the detector was 1279  
1233 tested with cosmic rays and electron beam. The detec- 1280  
1234 tor signal shows good uniformity along the vertical (Y) 1281  
1235 coordinate of the detector surface, but has a significant 1282  
1236 dependence in the horizontal (X) direction. Possible op- 1283  
1237 timization of this include a variable threshold and an op- 1284  
1238 timized selection of the PMTs installed on the right and 1285  
1239 left side of the detector. The response of the detector to 1286  
1240 particles is shown in Fig. 40. 1287

1241 The mean number of photo-electrons in saturation 1288  
1242 for the tray filled with  $n=1.030$  ( $n=1.020$ ) refractive in- 1289  
1243 dex aerogel is  $\sim 10$  ( $\sim 8$ ) which is close to expectation 1290  
1244 from Monte Carlo simulation. For the trays filled with 1291  
1245  $n=1.015$  and  $n=1.011$  refractive index aerogel, high 1292  
1246 numbers of photoelectrons were obtained with the use 1293  
1247 of higher reflectivity GORE material to cover the tray, 1294  
1248  $\sim 10$  and  $\sim 5.5$  respectively. This result could be fully re- 1295  
1249 produced by our Monte Carlo simulation by also assum- 1296  
1250 ing the aerogel absorption length on the order of 220 cm. 1297

### 1251 3.8.3. Results from tests with beam 1298

1252 The performance of the detector was tested with 1301  
1253 beam in Hall C. The detector signal showed good uni- 1302  
1254 formity along the vertical direction, but significant de- 1303  
1255 pendence in the horizontal direction. Possible optimiza- 1304  
1256 tions to address this are discussed below. The mean 1305  
1257 number of photoelectrons in saturation for a tray filled 1306  
1258 with  $n=1.030$  refractive index aerogel is 12 photoelec- 1307  
1259 trons and 10 for the tray filled with  $n=1.015$  refractive 1308  
1260 index aerogel (see Fig. 40). 1309

### 1261 3.8.4. Optimizations 1310

1262 Possible optimizations include a variable threshold 1312  
1263 and optimized selection of PMTs. Lower refractive in- 1313  
1264 dex and highly transparent aerogel like that currently 1314  
1265 under investigation by Aspen Aerogel, Inc. may allow 1315  
1266 to provide kaon proton distinction at even higher parti- 1316  
1267 cle momenta. 1317

## 3.9. Preshower and Shower Counters

### 3.9.1. Preface

The approved experiments demand a suppression of pion background for electron/hadron separation of 1,000:1, with suppression in the electromagnetic calorimeter alone on the level of 100:1. An experiment to measure the pion form factor at the highest  $Q^2$  accessible at JLab with 11 GeV beam requires a strong suppression of electrons against negative pions of a few 1,000:1, with a requirement on the electromagnetic calorimeter of a 200:1 suppression.

Particle detection using electromagnetic calorimeters is based on the production of electromagnetic showers in a material. The total amount of the light radiated in this case is proportional to the energy deposited by the primary particle in the medium. Electrons (as well as positrons and photons), will deposit their entire energy in the calorimeter giving the ratio of energy detected in the calorimeter to particle energy (energy fraction) of one.

Charged hadrons entering a calorimeter have a low probability to interact and produce a shower, and may pass through without interaction. In this case they will deposit a constant amount of energy in the calorimeter. However, they may undergo nuclear interactions in the radiator (in our case lead-glass) and produce particle showers similar to the electron and positron induced particle showers. Hadrons that interact inelastically near the front surface of the calorimeter and transfer a sufficiently large fraction of their energy to neutral pions will mimic electrons. The maximum attainable electron/hadron rejection factor is limited mainly by the cross section of such interactions.

In this section we describe details of construction of the SHMS calorimeter. We present results of pre-assembly component checkout, and performance from experimental studies.

### 3.9.2. Construction

As a full absorption detector, the SHMS calorimeter is situated at the very end of detector stack of the spectrometer [45]. The relatively large beam envelope of the SHMS dictated a design of a wide acceptance coverage. The general requirements for the SHMS calorimeter were:

- Effective area:  $\sim 120 \times 140 \text{ cm}^2$ ;
- Total thickness:  $\sim 20$  rad. length;
- Dynamic range: 1.0 - 11.0 GeV/c;
- Energy resolution:  $\sim 6\% / \sqrt{E}$ ,  $E$  in GeV;
- Pion rejection:  $\sim 100:1$  at  $P \gtrsim 1.5\text{-}2.0 \text{ GeV}/c$ ;
- Electron detection efficiency:  $> 98\%$ .

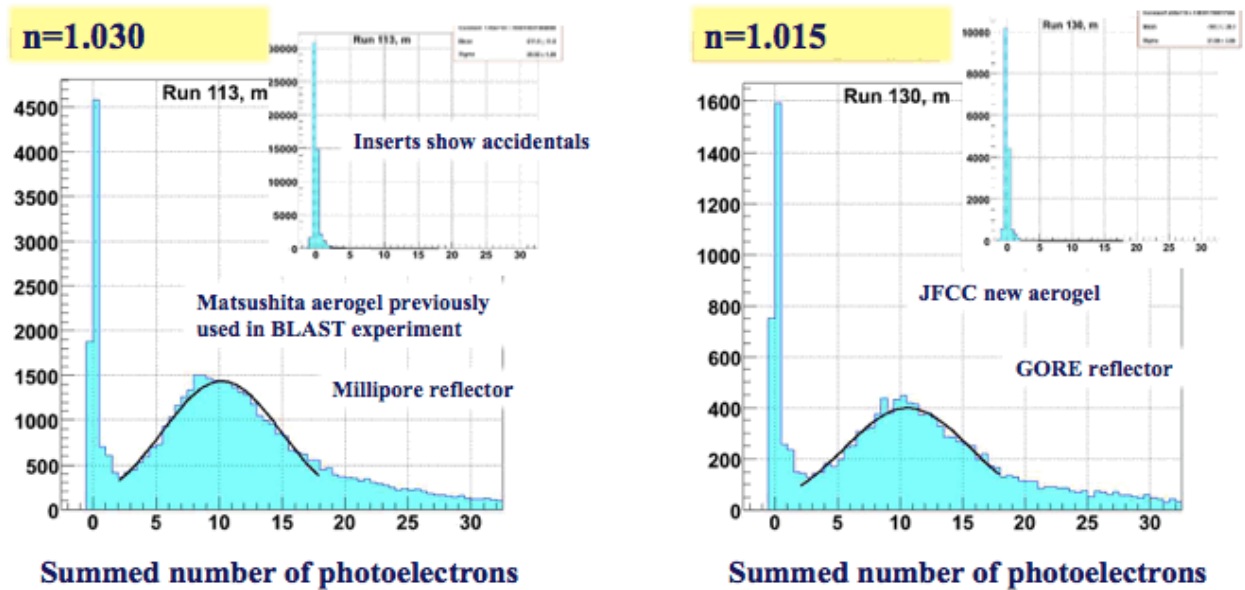


Figure 40: Numbers of photoelectrons observed in the Aerogel Cherenkov.

1318 The SHMS calorimeter consists of two parts (see  
 1319 Fig. 41): the main part at the rear (Shower), and  
 1320 Preshower before the Shower to augment PID capability  
 1321 of the detector.

1322 An optimal and cost-effective choice was found by  
 1323 using available modules from HERMES calorimeter for  
 1324 Shower part, and modules from the Hall C decommissioned  
 1325 SOS calorimeter for Preshower. With this choice  
 1326 the Shower became 18.2 radiation length deep and almost  
 1327 entirely absorbs showers from  $\sim 10$  GeV electromagnetic  
 1328 projectiles, and Preshower became 3.6 radiation length  
 1329 thick.

1330 The SHMS Preshower radiator consists of a layer of  
 1331 28 TF-1 type lead glass blocks stacked in two columns  
 1332 in an aluminum enclosure (not shown in Fig. 41). 28  
 1333 PMT assemblies, one per block, are attached to the left  
 1334 and right sides of the enclosure. The Shower part  
 1335 consists of 224 F-101 type lead glass modules stacked in  
 1336 a “fly’s eye” configuration of 14 columns and 16 rows.  
 1337 All blocks of Preshower were produced in early 1985-  
 1338 1990’s by a Russian factory in Lytkarino [49], whose  
 1339 products of good optical quality were well known.  $\sim$   
 1340  $120 \times 130$  cm<sup>2</sup> of effective area of detector covers the  
 1341 beam envelope at the calorimeter.

1342 The Preshower enclosure adds little to the material on  
 1343 the pass of particles. On the front and back are 2” Honeycomb  
 1344 plate and a 1 mm sheet of aluminum respectively, which  
 1345 add up to 1.7% of radiation length only.  
 1346 The optical insulation of the 10 cm  $\times$  10 cm  $\times$  70 cm  
 1347 TF-1 blocks in the Preshower is optimized to minimize

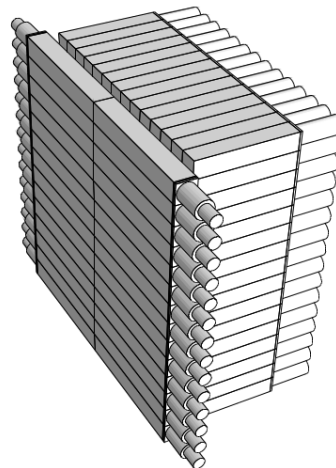


Figure 41: A sketch of SHMS calorimeter. Shown are Preshower (on the left) and Shower parts. Support structures are omitted.

1348 the dead material between them, without compromising  
 1349 the light tightness. First, the blocks are loosely wrapped  
 1350 in a single layer of 50  $\mu$ m thick reflective aluminized  
 1351 Mylar film, with Mylar layer facing the block surface.  
 1352 Then, every other block is wrapped with a 10 cm wide  
 1353 strip of 50  $\mu$ m thick black Tedlar film, to cover its top,  
 1354 bottom, left and right sides but the circular openings for  
 1355 the PMT attachments. Looking at the face of detector,  
 1356 the wrapped and unwrapped blocks are arranged in a  
 1357 checkerboard pattern. Insulation of the remaining front  
 1358 and back sides of the blocks are provided by facing in-

ner surfaces of the front and rear plates of the enclosure, covered also with Tedlar. In addition, a layer of Tedlar separates the left and the right columns.

The PMT assembly tubes are screwed in 90 mm diam. circular openings on both sides of the enclosure. The spacing of the openings matches the height of the blocks, so that a PMT faces to each of the blocks. The 3" XP3462B PMTs are optically coupled to the blocks using ND-703 type Bicon grease of refractive index 1.46.

The HERMES modules used in the Shower part are similar in construction to the HMS but differ in details. The radiator is an optically isolated  $8.9 \times 8.9 \times 50 \text{ cm}^3$  block of F-101 lead-glass, which is similar to TF-1 in physical parameters. The typical density of F-101 type lead-glass is  $3.86 \text{ g/cm}^3$ , radiation length 2.78 cm, and refraction index 1.65.

Results of TF-1 and F-101 type lead-glass blocks transmittance measurements are presented in [45].

Each F-101 block is coupled to a 3" XP3461 PMT from Photonis, with green extended bi-alkali photocathode, of the same sizes and internal structure as the XP3462B in the Preshower. Typical quantum efficiency of the photocathode is  $\sim 30\%$  for  $\lambda \sim 400 \text{ nm}$  light, and the gain is  $\sim 10^6$  at  $\sim 1500 \text{ V}$ . Silgard-184 silicone glue of refractive index 1.41 is used for optical coupling of the PMTs to lead-glass blocks.

A  $\mu$ -metal sheet of 1.5 mm thickness and two layers of Teflon foil are used for magnetic shielding and electrical insulation of the PMTs. The blocks are wrapped with  $50 \mu\text{m}$  aluminized Mylar and  $125 \mu\text{m}$  black Tedlar paper for optical insulation. A surrounding aluminum tube which houses the  $\mu$ -metal, is fixed to a flange, which is glued to the surface of the lead-glass. The flange is made of titanium, which matches the thermal expansion coefficient of F-101 lead-glass [46].

Beyond simple repairs, no adjustment has been made to the original HERMES construction of the modules for re-use in the SHMS calorimeter.

As both the TF-1 and F-101 lead-glass blocks have been in use for more than 14 years under conditions of high luminosity, there was concern about possible radiation degradation of the blocks and the PMTs.

The changes in transparency of TF-1 and F-101 type lead-glass radiators have been studied. The estimated radiation dose for the used blocks was about 2 krad. For several samples of F-101 and TF-1 type blocks the light transmittance has been measured before and after 5 days of curing with UV light (of wavelength  $\lambda=200\text{-}400 \text{ nm}$ ).

We did not find notable degradation in transmittance for the TF-1 type blocks taken from the SOS calorimeter and F-101 blocks taken from HERMES detector.

The gain and relative quantum efficiencies for randomly selected PMTs from the SOS calorimeter (XP3462B) and from the HERMES detector (XP3461) have been measured to check possible degradation effects in the PMTs. A  $\sim 10\text{-}15\%$  systematic decrease in quantum efficiency was noticed.

### 3.9.3. Photomultiplier tube selection and studies

The SHMS Preshower inherited PMTs from the retired SOS calorimeter. The choice of XP3462B PMT for Hall C calorimeters was made in 1994 after studies of several other 3 inch and 3.5 inch photomultiplier tubes on the matter of having good linearity, photocathode uniformity, high quantum efficiency, and good timing properties. Gain variations with HV and dark currents also were measured [50]. For samples of PMTs the photocathode uniformity and effective diameter have been studied with a laser scanner. Following these tests, as a time and cost effective solution, a 3" diameter ( $\approx 68 \text{ mm}$ ) semitransparent bi-alkaline photocathode, Photonis XP3462B PMTs were chosen for the equipment of the JLab Hall C calorimeters. These 8-stage PMTs have a linear focused cube dynode structure with a peak quantum efficiency (QE) of  $\sim 29\%$  at 400 nm.

### 3.9.4. Studies on optical properties of TF-1 type lead glass blocks

With its index of refraction  $\sim 1.65$ , radiation length 2.74 cm and density of  $3.86 \text{ g/cm}^3$  TF-1 type lead glass is well suited for serving as Cherenkov radiator in electromagnetic calorimeters. The fractional composition consists primarily of PbO (51.2%),  $\text{SiO}_2$  (41.3%),  $\text{K}_2\text{O}$  (3.5%) and  $\text{Na}_2\text{O}$  (3.5%).

The light transmittance of TF-1 type lead-glass blocks for the SHMS Preshower was checked in 2008 using a spectrophotometer from the JLab Detector Group [51]. The wave-length was scanned from 200 nm to 700 nm in steps of 10 nm. The blocks were oriented transversely, and the light intensity passing through the 10 cm thickness was measured. The results were compared with measurements from 1992, before assembling of calorimeters for the Hall C HMS/SOS spectrometers. Reliability of the measurements was checked by measuring spared, unused blocks and comparing again with 1992 data. From comparison of 1992 and 2008 data, signs of marginal degradation has been noticed.

### 3.9.5. Choice and studies of PMT bases

The Preshower PMT high voltage base design is optimized for the requirements of good linearity (better than 1%), high rate capability and a weak variation of PMT gain with anode current [50].

1460 A design, which is a purely resistive, high cur- 1508  
 1461 rent (2.3 mA at 1.5 kV), surface mounted divider 1509  
 1462 ( $\sim 0.640 M\Omega$ ), operating at negative HV is sel- 1510  
 1463 lected. The relative fractions of the applied HV 1511  
 1464 between the dynodes (from cathode to anode) are: 1512  
 1465 3.12/1.50/1.25/1.25/1.50/1.75/2.00/2.75/2.75. The sup- 1513  
 1466 ply voltage for a gain of  $10^6$  is approximately 1750 V. 1514

1467 The PMT resistive base assembly is linear to within 1515  
 1468  $\sim 2\%$  up to the peak anode current of  $120 \mu\text{A}$  ( $\sim 5 \times 10^4$  1516  
 1469 pe). The dark current is typically less than 3 nA. The 1517  
 1470 base has anode and dynode output signals. 1518

### 1471 3.9.6. Monte Carlo simulations 1522

1472 Prior to construction, the designed calorimeter setup 1523  
 1473 was computer simulated in order to possibly optimize 1524  
 1474 the setup and get predictions for key characteristics. 1525

1475 The simulations were based on the GEANT4 pack- 1526  
 1476 age [52], release 9.2. As in the simulations of the HMS 1527  
 1477 calorimeter (see [45]), the QGSP\_BERT physics list was 1528  
 1478 chosen to model hadron interactions [53]. The code 1529  
 1479 closely followed the parameters of the detector compo- 1530  
 1480 nents. Other features are added into the model in order 1531  
 1481 to bring it closer to reality, such as: light attenuation 1532  
 1482 length in the lead glasses and its block to block varia- 1533  
 1483 tion according to our measurements; PMT quantum ef- 1534  
 1484 ficiencies from the graphs provided by vendor, passive 1535  
 1485 material between the spectrometer focal plane and the 1536  
 1486 calorimeter; sampling of incoming particles at the focal 1537  
 1487 plane of the spectrometer. The Cherenkov light propa- 1538  
 1488 gation and detection was handled by a custom code, 1539  
 1489 in approximation of strict rectangular geometry of the 1540  
 1490 lead glass blocks with perfectly polished surfaces. Light 1541  
 1491 reflection and absorption by the Mylar wrapping was 1542  
 1492 modeled via Aluminum complex refractive index, with 1543  
 1493 Mylar support facing the block, and a thin air gap be- 1544  
 1494 tween the wrapping and the block. Both light passage 1545  
 1495 to the PMT photocathode through the optical grease 1546  
 1496 and the PMT window, and reflections from the block 1547  
 1497 sides were modeled in approximation of thin dielectric 1548  
 1498 layers ([54], p. 360). The electronic effects, such as 1549  
 1499 pedestal widths and channel to channel PMT gain vari- 1550  
 1500 ations were assumed as for the HMS calorimeter before 1551  
 1501 the 12 GeV modifications. 1552

1502 The simulations reveal no flaws in the design con- 1553  
 1503 struction of the SHMS calorimeter, and performance 1554  
 1504 similar to other lead glass based calorimeters. The stud- 1555  
 1505 ies indicated gain in pion suppression on the order of 1556  
 1506 several times from combining signal from Preshower 1557  
 1507 with total energy deposition in the calorimeter. 1558

### 3.9.7. Calorimeter Gain Matching

Gain matching of PMTs is important for uniformity of performance of the calorimeter over the spectrometer's acceptance. Minimum ionizing particles (MIP's) were used for this purpose, for their signals from the calorimeter nearly independent of particle's momentum.

MIP pion candidates for the Shower gain matching were selected by requesting 4 PMT signals from the Heavy Gas Cherenkov counter less than 2 p.e., and the normalized deposited in the Preshower energies close to the MIP peak value, within range from 0.02 to 0.15. In addition, the MIP dominance in the Shower itself was ensured by selecting single hit events, when only one module was fired. The resultant MIP peaks in the ADC signal distributions were localized by Gaussian fits (see Fig. 42).

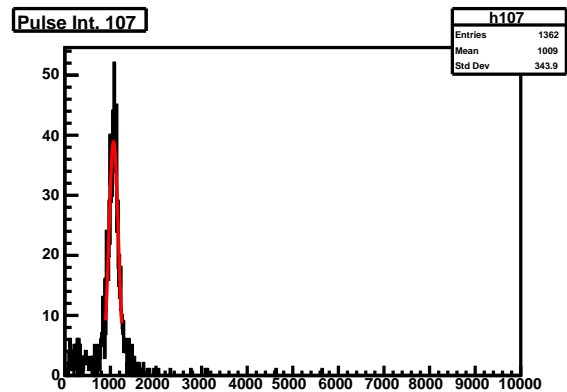


Figure 42: Distribution of ADC signals of a Shower module from minimum ionizing pions. The red line is a Gaussian fit to the MIP peak.

As gain matching had to be achieved by adjustment of high voltages on the PMT bases, knowledge of gain variations versus supplied HV's had been needed. That was obtained by measuring signals from MIP pions at 2 constant supply high voltages on all the Shower channels, at 1.4 kV and 1.5 kV (see Fig. 43). By assuming gain dependence on supplied voltage in the form  $\sim V^\alpha$  [19], the average exponent  $\alpha$  was found to be  $5.70 \pm 0.01$  for a set of  $\sim 100$  channels.

The gain matching was done in two ways. In the first case, MIP signals from pions were used. From the reference run with supply voltages  $A_{REF} = 1.4 \text{ kV}$  in all the Shower channels, MIP ADC signal amplitudes  $A_{REF}(i)$  were obtained as described above. For a desired constant signal amplitude  $A_{SET} = 1000 \text{ ADC}$  channels, the set voltages  $V_{SET}(i)$  were estimated via

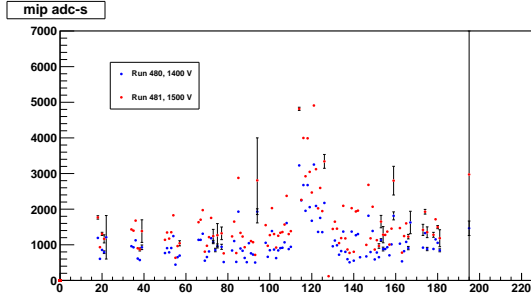


Figure 43: Amplitudes of ADC signals from MIP pions in a set of Shower channels, for supply voltages of 1.4 kV and 1.5 kV.

$$V_{SET}(i) = V_{REF} \cdot \left( \frac{A_{SET}}{A_{REF}(i)} \right)^{1/\alpha} \quad (5)$$

1540 In the second case, data from run of electron detec-  
 1541 tion in the SHMS were used. The SHMS optics was set  
 1542 up at 3 GeV/c central momentum, in a defocused mode,  
 1543 which allowed for hitting and calibration with electrons  
 1544 of more than 150 Shower modules. For deposited en-  
 1545 ergy  $E$  in a given module, signal amplitude  $A$ , PMT gain  
 1546  $g$ , calibration constant  $c$  the following holds:  $A \sim g \cdot E$ ,  
 1547  $E = c \cdot A$ . Hence  $g \sim V^\alpha \sim 1/c$ , and for the chosen  
 1548 calibration constant  $c_{SET}$  one gets

$$V_{SET}(i) = V_{REF} \cdot \left( \frac{c_{SET}^{-1}}{c_{REF}^{-1}(i)} \right)^{1/\alpha} \quad (6)$$

1549 The HV settings from the second method, for  $c_{SET} =$   
 1550  $35 \text{ MeV/ADC } ch$  are within the range from 1.2 kV to  
 1551 1.6 kV and are grouped around 1.4 kV (Fig. 44). A few  
 1552 settings above hard limit of 1.7 kV were forced to the  
 1553 limit. The HV settings from the two methods are in cor-  
 1554 relation.

1555 Note that out of acceptance hence not gain matched  
 1556 channels were left at nominal 1.4 kV high voltages.  
 1557 Note also that the chosen voltages are conservative, less  
 1558 than HV settings at which modules had been operated  
 1559 in the HERMES calorimeter.

1560 The amplitudes of ADC signals from MIP pions after  
 1561 the gain matching are shown in Fig. 45. The majority of  
 1562 amplitudes are grouped between 20 and 30 ADC chan-  
 1563 nels. The spread in signals among hit channels is much  
 1564 less than in the case of constant supply voltages (com-  
 1565 pare with Fig. 43).

1566 The Preshower detector was gain matched with cos-  
 1567 mic rays, prior to installation in the spectrometer. Coin-  
 1568 cidence of signals from scintillator counters positioned  
 1569 above and below the detector served as a trigger. The  
 1570 gain matching was adjusted after the installation, again

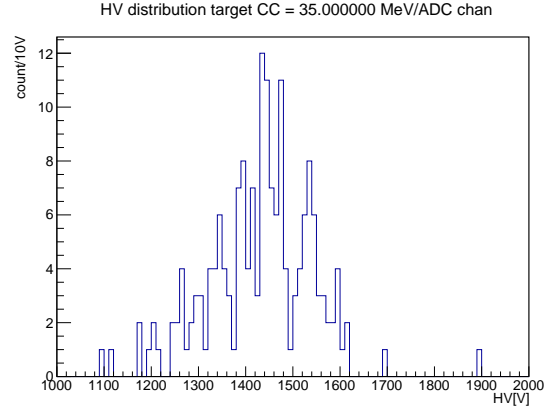


Figure 44: Gain matched high voltage settings for the Shower PMTs (see text for details).

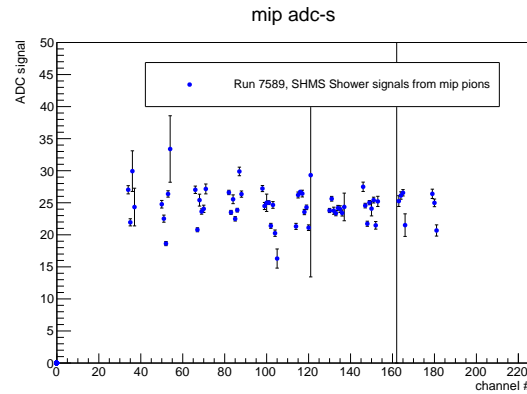


Figure 45: Amplitudes of ADC signals from MIP pions in a set of Shower channels after gain matching.

1571 with cosmics but this time passing through the detec-  
 1572 tor stack. Muons were identified as events of single  
 1573 track in the drift chambers and single hit module in the  
 1574 Preshower. New set of voltages were calculated based  
 1575 on MIP peak positions and according to formula simi-  
 1576 lar to Eqns 5, 6. The voltages span range from 1.1 kV  
 1577 to 1.7 kV. The quality of gain matching was insured by  
 1578 taking cosmic data with the new HV settings (Fig. 46).

### 3.9.8. Calorimeter Calibration

**To be updated. A representative plot from calibration to be added.**

The ability of particle identification of a calorimeter is based on differences in the energy deposition from different types of projectiles. The deposited energy is obtained by converting the recorded ADC channel value of each module into equivalent energy.

The data analysis procedure corrects for the gain dif-

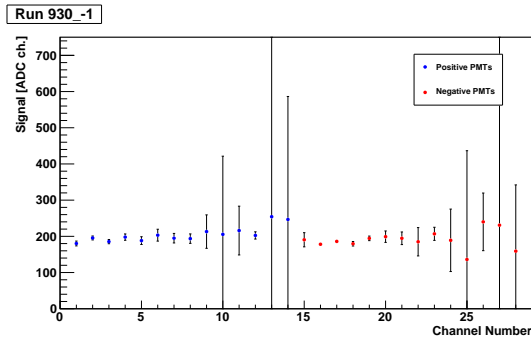


Figure 46: Amplitudes of ADC signals from cosmic muons in the Preshower channels after gain matching.

ferences in the process of calorimeter calibration. Good electron events are selected by means of gas Cherenkov detector. The standard calibration algorithm [55] is based on minimization of the variance of the estimated energy with respect to the calibration constants, subject to the constraint that the estimate is unbiased (relative to the primary energy). The momentum of the primary electron is obtained from the tracking in the magnetic field of the spectrometer.

The deposited energy per channel is estimated by

$$e_i = c_i \times A_i, \quad (7)$$

where  $i$  is the channel number,  $c_i$  is the calibration constant,  $A_i$  is the FADC pulse integral signal. Note that the Preshower signals are corrected for the light attenuation dependence versus horizontal hit coordinate  $y$ .

In the calorimeter analysis code hits on adjacent blocks in the Preshower and in the Shower are grouped into clusters. For each cluster the deposited energy and center of gravity are calculated. These clusters are matched with tracks from the upstream detectors if the distance from the track to cluster is less than a predefined “slop” parameter (usually 7.5 cm). For the Preshower the distance is calculated in the vertical direction.

The calorimeter energy corresponding to a track is divided by the track momentum and used for particle identification. In the few GeV/c range pions and electrons are well separated (see Fig. ??, NEED FIGURE), a cut at 0.7 ensures an electron detection efficiency ~99% and pion suppression of tens of times.

### 3.9.9. Summary on the SHMS calorimeter

Design, construction details and performance of the electromagnetic calorimeter for the newly built SHMS spectrometer in Hall C has been presented. From a few

considered versions, the Preshower+Shower configuration was selected as most cost-effective. The Preshower consists of a layer of 28 modules with TF-1 type lead glass radiators, stacked back to back in two columns. The Shower part consists of 224 modules with F-101 type lead glass radiators, stacked in a “fly eye” configuration of 14 columns and 16 rows.  $120 \times 130 \text{ cm}^2$  of active area covers beam envelope at the calorimeter.

The calorimeter was commissioned as part of the SHMS detector package in the fall of 2017, then used in the first 12 GeV Hall C experiments in 2018. The first calorimeter data show satisfactory performance of the detector.

## 4. Trigger and Data Acquisition

The Hall C data acquisition (DAQ) system is designed to meet the needs of a high luminosity, dual spectrometer (SHMS + HMS) configuration, with the capability of extracting polarization-dependent absolute cross sections with precision at the 1% level or better. JLab’s CODA data acquisition software [65] provides a framework that ties together a distributed network of read-out controllers (ROCs) controlling multiple crates of digitization hardware, event builders to serialize the data, and event recorder processes to write the data to disk. It also provides a graphical control interface for the users.

The Hall C DAQ system can run in dual-arm trigger mode that requires a coincidence between both spectrometers, or each arm’s DAQ may be run entirely independently of the other. Incorporating additional detector systems into the standard two-arm design is also straightforward. A high-level block diagram of trigger formation and readout for each spectrometer arm (SHMS or HMS) is depicted in (Fig. 47).

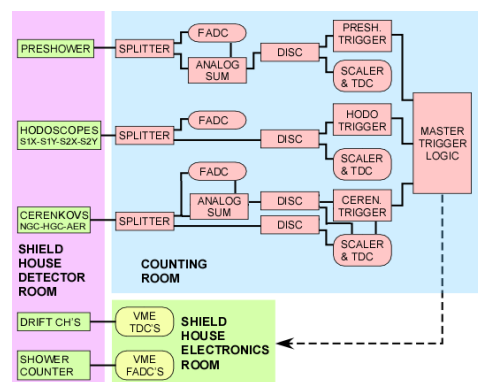


Figure 47: Block diagram of high-level trigger formation for SHMS (and HMS). See Section 4.1 for details.

The hardware DAQ and trigger designs were strongly influenced by the preceding 6 GeV HMS and SOS configurations. This choice was made to provide a careful and systematic migration from the very well understood systematics of the 6 GeV system while incorporating and characterizing a new generation of FPGA-based logic and readout electronics. To this end, the present system relies on a combination of *legacy* NIM and CAMAC discriminators and logic modules to form readout triggers, but utilizes a full set of modern high speed payload and front-end modules to allow a transition to a firmware based trigger and fully pipelined readout in the future.

In the present configuration, the DAQ has a nominal maximum trigger accept rate of 4 kHz with a dead-time of  $\approx 20\%$ . Dead times are measured using the Electronic Dead Time Measurement system outlined in Section 4.2. The underlying hardware supports running in a fully pipelined mode, and should be capable of running at trigger rates exceeding 20 kHz with minimal dead-time using firmware based triggers similar to those employed in Halls B and D. This capability was not part of the initial 12 GeV upgrade plan for Hall C, but may be pursued in the future (Sect. 4.5).

Signals from the scintillator planes, Cherenkov detectors, and Calorimeter detectors in the SHMS and HMS detector stacks are processed to form *pre-triggers*. Those pre-triggers can serve as *event triggers* themselves (that initiate a recorded event), or be combined to bias data collection towards particular particle types (*i.e.* electrons *vs.* pion) and suppress backgrounds. Each running DAQ can be fed up to six independent triggers simultaneously and the Experimenter can control what fraction of each is recorded to disk run-by-run through an integrated pre-scale feature.

#### 4.1. Standard Triggers

All trigger-related PMT signals from both the SHMS and HMS are routed out of the experimental Hall to a dedicated electronics room on the main level of the Hall C Counting House using low-loss RG-8 air-core signal cables. Those signals are then split with one copy running into a JLab F250 flash analog to digital converter (FADC)[66], and the second copy is processed and discriminated. All discriminated pulses are delivered to scalers for rate information, TDCs for precision timing measurement, and to form pre-triggers as described below. This design allows direct access to all raw signals that may participate in a trigger during beam operations and has proven invaluable during the debugging and commissioning phases of Hall operations.

Non-trigger related signals include wire-chamber readouts and the Shower (but not Pre-Shower) layer of the SHMS calorimeter. The readout electronics for those sub-detectors remain inside their respective detector huts within the experimental Hall. All SHMS Calorimeter PMT signals are fed into F250 FADCs configured to provide timing, integrated energy, pulse amplitude, and (optionally) pulse profile data as desired. The wire-chamber timing signals are digitized using multi-hit CAEN v1190 modules [67].

The CAEN v1190 payload module provide 128 independent multi-hit/multi-event TDC channels with a user configurable resolution ranging from  $52\ \mu\text{s}$ —100 ps per bin. They provide a 32 kilo-word deep output buffer and can be readout asynchronously with respect to the event triggers. Typical Hall C operation has all units configured for 100 ps/bin.

##### 4.1.1. JLab F250 Flash ADCs

The JLab F250 flash ADC modules are an FPGA-based design developed by the Jefferson Lab Fast Electronics group [66] and are used Lab wide. Each F250 module provides 16 independent  $50\ \Omega$  input channels. The voltage at each input channel is continuously digitized into an  $8\ \mu\text{s}$  ring buffer at 250 MHz, with a resolution of 12 bits, and a hardware adjustable full-scale range. When a modules receives a readout trigger, digitized sample data stored in the ring buffer is processed in a parallel process that does not incur front-end deadtime. In typical operation each ‘hit’ over a pre-programmed threshold is assigned an interpolated leading-edge threshold time ( $<1\ \text{ns}$  resolution), integrated energy (analogous to a charge-integrating ADC value), a peak-amplitude, and a measurement of any DC offset (pedestal) present on the channel prior to the detected pulse. Full pulse-profile data for each hit may also be stored if desired. However, that mode increases the data rate by several orders of magnitude, and is generally used only for debugging or limited duration pulse characterization runs.

##### 4.1.2. SHMS Triggers

The SHMS detector stack layout is described in Section 3.2. A representative detector layout is presented in Figure 48.

Each hodoscope plane described in Sections 3.3 and 3.4 is constructed from an array of horizontal (or vertical) bars with a PMT on each end. Signals from those PMTs are split and one analog copy is delivered to F250 FADCs. The second analog copy is discriminated and sent to CAEN 1190 TDCs for precision timing information, to scalers for raw rate information, and to logic

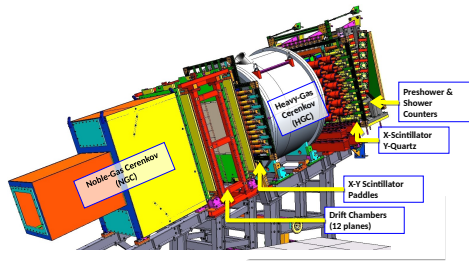


Figure 48: Typical detector layout for the SHMS.

modules to provide the hodoscope pre-triggers plane by plane. A pre-trigger for each plane generated by OR'ing the discriminated signals from each side of a hodoscope plane together, then AND'ing the resulting two signals together. The pre-triggers are designated S1X, S1Y and S2X, S2Y; where 1(2) denote the up(down)stream plane, and X(Y) denote the horizontal(verical) scintillator bar orientation (Fig. 49).

It should be noted an optimal design would generate an AND between the PMTs on each side of every bar first, and OR the resulting per-bar coincidences to form a pre-trigger for the plane. The compromise above was driven by constraints of the legacy LeCroy 4564 CAMAC logic units held over from the 6 GeV era.

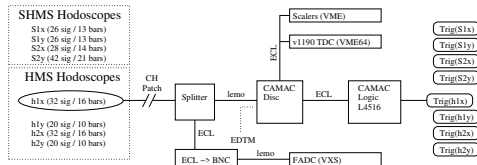


Figure 49: Block diagram for SHMS and HMS hodoscope pre-trigger formation.

The SHMS detector stack includes a permanent Heavy Gas Cherenkov (HGC) (Sect. 3.6), but also includes space for a second Noble Gas Cherenkov (NGC) (Sect. 3.7). Each SHMS gas Cherenkov detector incorporates four PMTs, each detecting light from one of four mirrors inside their respective gas volumes. Analog signals from the PMTs are split (50:50) with one path plugged into an FADC. The second copies from each PMT are summed, and the summed output is discriminated to form a Cherenkov pre-trigger for that Cherenkov detector (HGC and NGC). The pre-triggers are also routed to scaler channels and a v1190 TDC.

An optional SHMS Aerogel (Sect. 3.8) may also be installed. It employs seven PMTs on each side of its dif-

fusion box. The signals from all 14 PMTs are handled analogous to the gas Cherenkov, with each analog signal being split and readout by an individual FADC channel, and second copies being summed and discriminated to form an associated aerogel pre-trigger. The pre-trigger is routed to a scaler and v1190 TDC as well.

A block diagram for the Cherenkov pre-triggers is presented in Figure 50.

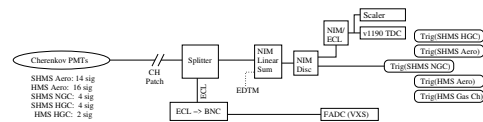


Figure 50: Block diagram for SHMS and HMS Cherenkov pre-trigger formation.

The SHMS PreShower layer (Sect. 3.9) consists of 28 lead-glass blocks arranged 14 rows, with 2 blocks to a row. Each block is coupled to a single PMT on the side facing the perimeter of the layer. Analog signals from the 28 PMTs are split and summed in 3 groups of 4 rows, and 1 group of 2 rows. Each of the 4 group sums is readout by an FADC channel for cross checks. The 4 group sums are summed in turn to provide a total PreShower sum which is then discriminated and provides the SHMS *PSh* pre-trigger. Provision is made to generate independent pre-triggers for both low- and high- energy depositions in the PreShower layer (*PSh<sub>Lo</sub>* and *PSh<sub>Hi</sub>*, respectively) (Fig. 51).

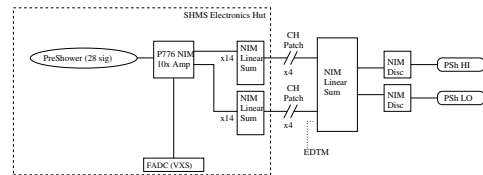


Figure 51: Block diagram for SHMS PreShower summing trigger.

The aforementioned pre-triggers are then combined to form a set of triggers capable of initiating a DAQ event. These combination are often adjusted or optimized to serve the needs of particular experiments but a set of commonly available event triggers is outlined in Section 4.1.4.

#### 4.1.3. HMS Triggers

The standard HMS detector stack [69] is the predecessor of the SHMS system and shares a nearly identical design (Fig. 52). It consists of a pair of scintillator-based hodoscope planes in an X+Y configuration, a gas Cherenkov detector, a second pair of X+Y hodoscopes, and a Preshower + Shower Calorimeter. Provision is

1816 also made for an optional Aerogel Cherenkov to be inserted  
 1817 into the detector stack just downstream of the drift chambers  
 1818 for supplemental particle identification (PID).

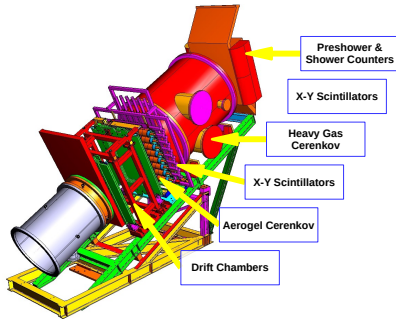


Figure 52: Typical detector layout for the HMS.

1819 The trigger and readouts designs follow the patterns  
 1820 described in Section 4.1.2, with a modest difference associated  
 1821 with the HMS Calorimeter.  
 1822

1823 Signals from the four HMS hodoscope planes, denoted  $h1x$ ,  $h1y$ ,  $h2x$ ,  $h2y$ ,  
 1824 are split, discriminated, and recombined to form a *Scin* trigger following the same  
 1825 logic as the SHMS hodoscopes described previously.  
 1826

1827 The HMS gas Cherenkov detector incorporates two  
 1828 PMTs detecting light from two mirrors inside the HMS Cherenkov tank.  
 1829 Analog signals from the PMTs are split (50:50) with one path plugged into an FADC.  
 1830 The second copies from each PMT are summed, and the summed output is discriminated  
 1831 to form the Cherenkov pre-trigger. That pre-trigger is also routed to a scaler  
 1832 and v1190 TDC.  
 1833

1834 The HMS Aerogel employs eight PMTs on each side  
 1835 of its diffusion box. The signals from all 16 PMTs are split and readout by an  
 1836 individual FADC channel, with the second copies being summed and discriminated  
 1837 to form the associated aerogel pre-trigger. The pre-trigger is routed to a scaler  
 1838 and v1190 TDC as well.  
 1839

1840 The HMS calorimeter is composed of four layers of  
 1841 lead glass blocks. Each layer has 13 lead-glass blocks arranged horizontally, and the  
 1842 layers are denoted A, B, C and D as seen by a particle passing through the detector  
 1843 stack. Layers A and B have PMTs bonded to each end of their blocks, while Layers  
 1844 C and D have a single PMT on one side only. Analog signals from the PMTs are  
 1845 split 50:50 with one copy being delivered to an FADC. The copies are formed into  
 1846 an analog sum for each side of each layer, denoted  $hA+$ ,  $hA-$ ,  $hB+$ ,  $hB-$ ,  $hC$ , and  
 1847  $hD$ . Layer sums  $hA$  and  $hB$  are formed by summing  $hA+$  and  $hA-$ , and  $hB+$  and  
 1848  $hB-$ , respectively ( $hC$  and  $hD$  are already layer sums).  
 1849

1853 and  $hD$  are already layer sums).

1854 One copy of each layer sum is sent to an FADC for monitoring and cross checks.  
 1855 A PreShower pre-trigger is formed by summing and discriminating Layers A + B,  
 1856 and a *Shower Low* pre-trigger is formed by summing and discriminating Layers  
 1857 A+B+C+D. Copies of the PreShower and Shower sums are sent to FADCs and  
 1858 copies of the discriminated pre-trigger signals are sent to scalers and 1190 TDCs.  
 1859

1860 Figure 53 depicts a block diagram of the HMS Calorimeter pre-triggers.  
 1861  
 1862  
 1863

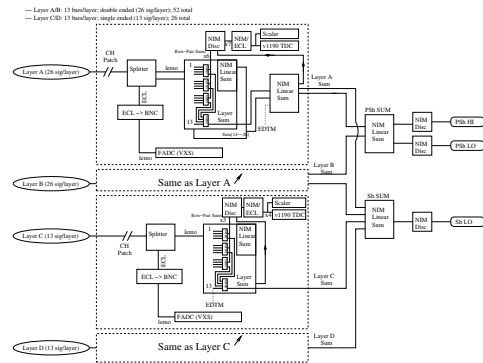


Figure 53: Block diagram for HMS Shower and Preshower summing triggers.

#### 4.1.4. Event Triggers

The aforementioned pre-triggers are then combined to form a set of triggers capable of initiating a DAQ event. The ‘default’ single-arm trigger is formed by 3 out of 4 hodoscope planes firing in coincidence. Often referred to as the *3 of 4* or *Scin* trigger, it provides a high-efficiency (> 99%) general-purpose charged particle trigger.

A second standard trigger is referred to as *EL\_Clean*. It implements particle discrimination at the trigger level by forming a coincidence between the *Scin* pre-trigger, one (or more) Cherenkov pre-triggers, and (optionally) the pre-shower (*PSh*) and/or calorimeter total-sum (*ShTot* pre-triggers).

#### 4.2. Electronic Dead Time Measurement System (EDTM)

The DAQ and trigger system for each spectrometer also includes an Electronic Dead Time Measurement (EDTM) system. This is implemented by replicating a pulse from a pulse-generator circuit and feeding into every pre-trigger leg as close to the analog signals as possible. The timing of those duplicated pulses is adjusted to match those generated by a real particle passing through the detector stack. A copy of each synthetic

1888 EDTM trigger is counted in a deadtime free scaler and 1935  
1889 sent to a dedicated TDC channel in each arm. The pres- 1936  
1890 ence of an appropriately timed hit in that TDC channel 1937  
1891 tags an event as having been generated by an EDTM 1938  
1892 trigger. 1939

1893 During beam operations, this allows a direct measure- 1940  
1894 ment of the fraction of triggers that are lost due to some 1941  
1895 component of the DAQ being busy. This is known as 1942  
1896 the system *deadtime*. By inducing synthetic signals as 1943  
1897 early in the trigger electronics as possible, this system 1944  
1898 is sensitive to high-rate signal pile-up in the full front- 1945  
1899 end trigger logic chain, as well as digitization and read 1946  
1900 out related deadtimes implicit in the non-pipelined DAQ 1946  
1901 operation presently in use in Hall C.

1902 In addition to the above function, the system has 1947  
1903 proved useful for pre-beam trigger verification and end 1948  
1904 to end checkout of the DAQ system. 1949

- 1905 • It allows rough timing on all trigger legs to be ver- 1951  
1906 ified without beam. 1952
- 1907 • It allows coincidence timing between the SHMS 1954  
1908 and HMS arms to be roughed in and tested without 1955  
1909 beam. 1956
- 1910 • It allows the entire DAQ system to be stress tested 1957  
1911 under controlled conditions without beam. 1958

### 1912 4.3. Auxiliary Data Collection 1960

1913 The standard method for slow controls data logging is 1962  
1914 through the Experimental Physics and Industrial Con- 1963  
1915 trol System (EPICS)[64]. EPICS is a system of open 1964  
1916 source software tools and applications used to pro- 1965  
1917 vide control user interfaces and data logging for sys- 1966  
1918 tems such as high- and low-voltage detector power sup- 1967  
1919 plies, target systems, spectrometer magnets, vacuum, 1968  
1920 and cryogenic systems, etc. 1969

1921 Long-term, persistent storage of EPICS based slow 1970  
1922 controls data is provided through an independent archiving 1971  
1923 system managed by the Accelerator Division’s MYA 1972  
1924 archiving system. A experimentally relevant subset of 1973  
1925 EPICS data (beam and target characteristics; magnet, 1974  
1926 spectrometer and detector settings, etc.) are also stored 1975  
1927 in the experimental data files at regular intervals when- 1976  
1928 ever the DAQ is running. 1977

### 1929 4.4. Online Hall C Computing Environment 1978

1930 Hall C employs a dedicated stand-alone computing 1978  
1931 cluster with redundant multi-core servers focused on 1979  
1932 prompt online analysis, high volume local data stor- 1980  
1933 age, and 1–10 Gb ethernet interconnects. There are 1981  
1934 dedicated hosts for each independent DAQ system (*ex.* 1982

SHMS and HMS), and auxiliary machines for polarime-  
try, target controls, spectrometer slow controls, etc.

Experimental control and operational feedback is provided to users in the Hall C Counting house through a collection of multi-screen computer workstations and a set of large wall-mounted displays for critical data.

All systems have direct access to the JLab centrally managed Scientific Computing resources. This includes multi-petabyte tape storage and online disk facilities, as well as a several thousand core compute farm for simulation and offline data analysis[68].

### 4.5. Future Plans / Pipeline trigger

During the early stages of the 12 GeV Hall C upgrade plan it was concluded that the risks of moving to a fully pipelined DAQ system with a firmware driven trigger were not justified by the needs of the initial experimental program. In general, those experiments did not impose a too heavy burden on the DAQ, and the more conventional trigger design with its well understood characteristics was preferred.

However, provision was made to design and build the low-level DAQ system with an upgrade path in mind. To that end, a full compliment of trigger and payload modules compatible with the pipelined systems being implemented for Halls B and D was selected.

A phased transition from the NIM/CAMAC trigger system to a fully pipelined approach would involve implementing the present trigger logic within the existing JLab FADC and VXS Trigger Processor (VTP) boards, and a thorough validation of the firmware based trigger decisions against the well understood conventional trigger. Once the firmware is fully debugged/characterized, the DAQ could transition to pipelined mode and take advantage of significant boost in trigger accept rates into the 10’s of kHz range with minimal deadtime. At that point the next DAQ bottleneck would likely be rate limitations in the detector systems themselves (signal pile-up in the front-end, track reconstruction limitations, etc.)

## 5. Software

Hall C Data is analyzed by the Hall C analysis package *hcana*. This package does full event reconstruction for the SHMS used alone or in coincidence with other detectors. *hcana* is based on the modular Hall A analyzer [62] ROOT [63] based C++ analysis framework. This framework provides for run time user configuration of histograms, ROOT tree contents, cuts, parameters and detector layout.

hcana includes C++ classes for detectors, spectrometers, and physics analyses. Instantiation of these classes as objects is configured at run-time through a ROOT script which also sets up the configuration of analysis replay. Due to the similarity of the SHMS and HMS spectrometers and their detector packages, the same spectrometer and detector classes are used for both spectrometers. For example, the drift chamber package class is instantiated for both spectrometers with each object configured by its specific parameters and geometry. Additional modules such as new front end decoders, detectors, or physics analysis modules can easily be added to hcana. These modules can either be compiled into the analyzer or be compiled separately and dynamically loaded at run time.

Event analysis is segmented into 3 steps of spectrometer and detector specific analysis.

1. Decoding: Detector requests from the low level decoder a list of hits sorted detector by plane and counter number. A minimal amount of processing is done to make data available for low level histograms.
2. Coarse Processing: Tracks are found in the drift chambers. Hits and clusters in the hodoscope, shower counter and other detectors are matched to the tracks to determine time-of flight. The various detectors provide information for particle identification.
3. Fine processing: Particle identification information is refined, tracks in the focal plane are traced back to the target coordinate system and particle momentum is determined.

Each step of these steps is completed for all detectors before proceeding to the next step. Some limited information is passed between detectors at each step. For example, timing information from the hodoscopes is used to obtain the start time for the the drift chambers in the decoding step and tracks obtained from the drift chambers are associated with shower counter hit clusters in the fine processing step.

After these steps single arm and coincidence physics quantities are calculated using various physics analysis classes that are configured at run-time.

### 5.1. Online Monitoring

After each data taking run (typically an hour or less) is started, a subset of the data is analyzed with hcana. An easily configurable histogram display GUI is used to view diagnostic histograms and compare them to reference histograms. The EPICS [64] control system alarm

handler is used to monitor experiment settings and beam conditions. This includes spectrometer magnet settings, detector high voltages, drift chamber gas, cryogenic systems and spectrometer vacuum.

## 6. SHMS Performance: Operating Experience and Commissioning Results

*System Performance section. Organizer: Editors – with input from all authors.*

### 6.1. Acceptance

The acceptance of the SHMS can be determined from simulation and defined as  $A(\delta, \theta) = N_{sus}(\delta, \theta)/N_{gen}(\delta, \theta)$ , where  $N_{gen}$  is the number of events generated into a particular  $\delta, \theta$  bin and  $N_{sus}$  is the number of events that successfully reached the detector stack. Since  $A(\delta, \theta)$  depends on the generation limits of the simulation, a more useful quantity is the effective solid angle,  $\Delta\Omega_{eff} = A(\delta, \theta) * \Delta\Omega_{gen}$ , where  $\Delta\Omega_{gen}$  is the solid angle generated into for each bin. Figure 54 shows the effective solid angle of the SHMS at a central angle of  $21^\circ$  and central momentum of  $3.3 \text{ GeV}/c$  for a 10 cm liquid hydrogen target.

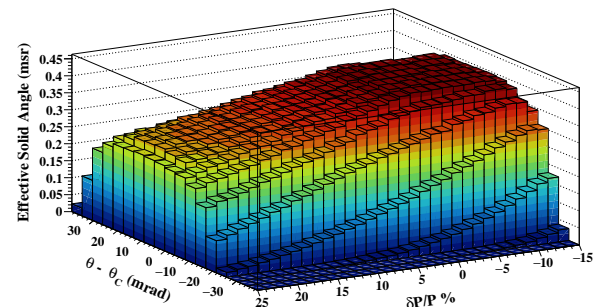


Figure 54: SHMS effective solid angle as a function of  $\delta P/P$  and  $\theta$ . SHMS  $\theta_{central} = 21^\circ$  and  $P_{central} = 3.3 \text{ GeV}/c$ .

Figure 55 shows the position and angular distribution of tracks formed from the drift chambers at the focal plane. The plots on the left are from simulation and data is on the right. The red lines represent the edges of the distributions, determined from the simulation, and are meant to guide the eye when comparing data and simulation. A good agreement between the two reflects our understanding of both the magnetic forward transport and physical locations of the apertures which determine the acceptance.

Figure 56 is a simulation versus data comparison of the target variables  $Y_{tar}$ ,  $Y'_{tar}$ ,  $X'_{tar}$ , and  $\delta$  that were described in section 3.1. After subtracting the Al cell walls

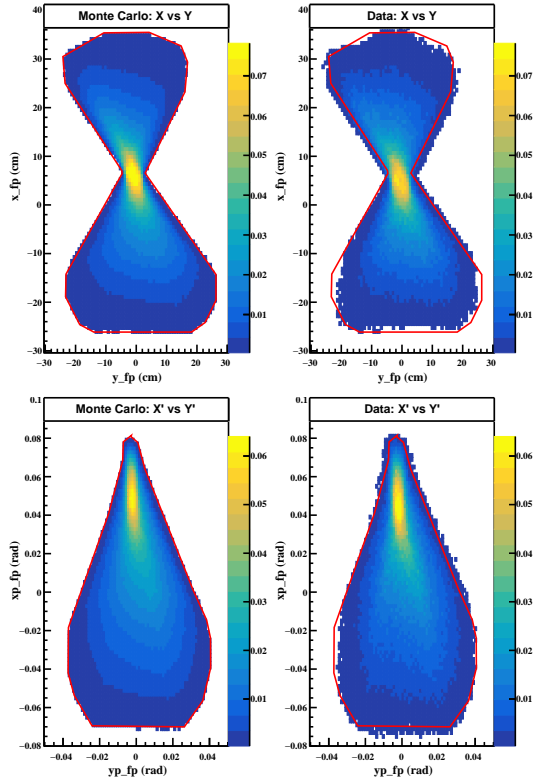


Figure 55: Comparison of focal plane quantities, simulation is on the left and data is on the right. The top plots are the position at the focal plane and the bottom is the angles at the focal plane determined from tracks formed by the drift chamber planes. The red outline represents the expected shape determined from simulation.

2066 (black histogram) of the hydrogen target using dummy  
 2067 foil data, the agreement between data (blue histogram)  
 2068 and Monte Carlo (red histogram) is reasonable.

2069 To demonstrate how large of the SHMS acceptance is  
 2070 in  $Y_{tar}$ , one look at optics data taken during the A1N  
 2071 experiment. Figure 57 plots with reconstructed position  
 2072 along the beam line,  $z_{tar}$  ( which was reconstructed us-  
 2073 ing the measured and  $Y'_{tar}$ ).

## 2074 6.2. Rates and Livetime

### 2075 6.2.1. Deadtime Measurement by Electronic Pulse 2076 Generator

The computer live time efficiency of the DAQ is de-  
 fined as,

$$\epsilon_{CLT} = \frac{N_{(phy+edtm),TDC} - N_{(edtm),TDC}}{N_{(phy+edtm),SCL} - N_{(edtm),SCL}} \quad (8)$$

where the numerator is the total number of EDTM-  
 subtracted TDC counts (total accepted physics triggers)  
 and the denominator is the total number of EDTM-  
 subtracted scaler counts (total physics pre-triggers).

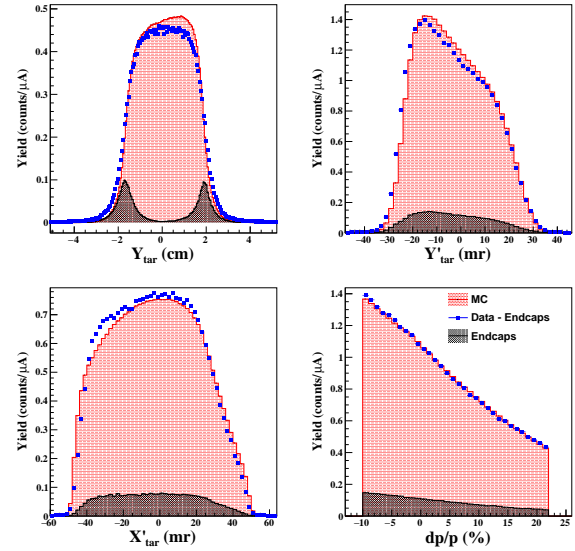


Figure 56: Target variable comparison of data versus Monte Carlo simulation from [56]

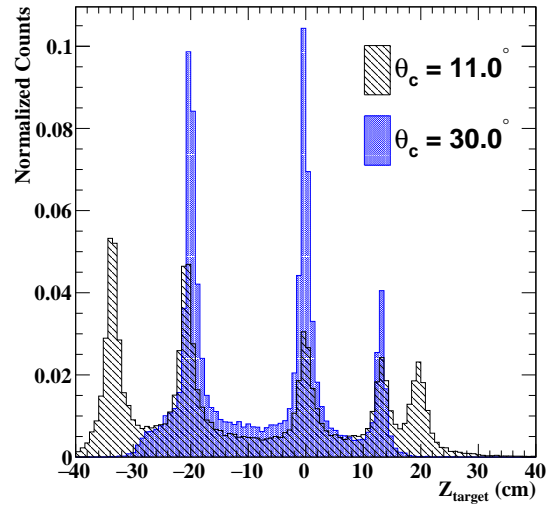


Figure 57: Reconstructed  $z_{tar}$  for a carbon foil optics target at SHMS central angles of  $11^\circ$  and  $30^\circ$ . Carbon foils were located at approximately -20, 0, 13.3 and 20.0 cm. The peak located at -35 cm is from the beam pipe exit window. The target chamber was not under vacuum and therefore a background from air is present in the data and not subtracted here

The EDTM introduces a bias in the computer live time calculation and must therefore be subtracted from the physics trigger. The bias comes from the fact that the the EDTM is a clock and cannot be blocked by another EDTM signal, thereby having no contribution to

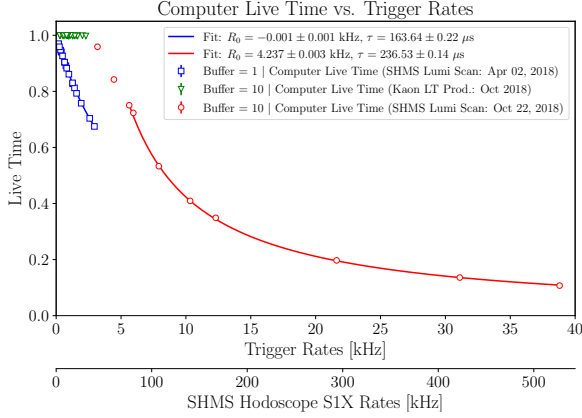


Figure 58: Computer live time vs. trigger rates (top x-axis) and SHMS hodoscope SIX plane rates (bottom x-axis) for DAQ buffer levels 1 and 10.

the deadtime of the system. An additional bias arises during beam-off time periods, where only EDTM triggers are counted. To remove this bias, a beam current cut was required in the live time calculation.

The computer live time data shown in Figure 58 is plotted against the un-prescaled input trigger rates (top x-axis) and the first plane (SIX) of the SHMS Hodoscopes (bottom-axis). The data were obtained from the SHMS luminosity scans and the Kaon LT experimental data taken on Fall 2018. The Spring 2018 scans (blue squares) were taken with DAQ in buffer level 1 (unbuffered mode) and the Kaon LT data (green triangles) and Fall 2018 scans (red circles) were with DAQ in buffer level 10 (buffered mode). The advantage of buffered mode (technical definition should be described in another section) is that the DAQ is capable of accepting higher trigger rates while keeping the computer live time efficiency  $\sim 100\%$ . Both buffered and unbuffered modes exhibit a characteristic fall-off of the live time as a function of the trigger rate which has been modeled using the fit function,

$$f_{\text{CLT}}(R) \equiv \frac{1}{1 + (R - R_0)\tau}, \quad (9)$$

where  $R$  is the input trigger rate,  $R_0$  describes a horizontal offset between the unbuffered and buffered modes and  $\tau$  represents the averaged data readout time (dead-time) before the DAQ is ready to accept another pre-trigger. The fit function, however, is unable to describe the “flat” region where the live time is nearly 100%. From the fit parameters, the fall-off behavior of buffered mode starts at trigger rates,  $R \sim 1/\tau$ , which corresponds to a numerical values of  $\sim 4.2$  kHz before a significant drop in the live time is observed.

As of Fall 2018, the DAQ has been operated in buffered mode which has proved to be more feasible for current and future high-rate experiments at Hall C.

### 6.3. System Efficiency

#### 6.3.1. HGC Performance

The performance of the HGC is determined by the capacity to separate particle species on the basis of produced NPE. In particular, the HGC is a threshold Cherenkov detector and thus identifies species based on whether or not a signal greater than 1.5 NPE was generated or not. The first metrics of performance to be discussed are the detector efficiency and contamination.

Efficiency in this context refers to the ratio of events selected as a particular particle species by all detectors in the SHMS, including the HGC, over the number of events selected as that same species without any information from the HGC. This is illustrated by the equation

$$\eta_{\text{HGC}} = \frac{\pi^+ \text{ detected with HGC signal}}{\pi^+ \text{ detected without HGC signal}}, \quad (10)$$

where  $\eta_{\text{HGC}}$  represents the detector efficiency of the HGC and  $\pi^+$  particle type is used as an example. The selection criteria includes cuts on the timing information, reconstructed  $\beta$ , calorimeter, aerogel and HGC information, and a single reconstructed track. Contamination refers to the number of events identified as a sub-threshold particle by the calorimeter and aerogel Cherenkov, but produced more than 1.5 NPE in the HGC. For example, if the HGC is configured for  $\pi^+/K^+$  separation, the  $K^+$  contamination is defined as the number of events identified as a  $K^+$  by all detectors, except the HGC, which identified a  $\pi^+$ .

Two runs are chosen to show HGC efficiency and contamination, one where the HGC separated between  $e^-/\pi$  and the other  $\pi/K$ . The former featured the HGC filled with  $\text{CO}_2$  at 1 atm and a SHMS central momentum of  $-3.0 \text{ GeV}/c^2$ . Particle identification was established by a cut on the normalized calorimeter energy. The latter had the HGC filled with  $\text{C}_4\text{F}_{10}$  at 1 atm, giving a  $\pi$  momentum threshold of  $2.8 \text{ GeV}/c^2$  and a  $K$  momentum threshold of  $9.4 \text{ GeV}/c^2$ , at a SHMS central momentum

PID Configuration	Efficiency	Contamination
$e^-/\pi^-$	95.99%	10000 : 1
$\pi^+/K^+$	98.22%	1000 : 1

Table 5: Summary of the Heavy Gas Cherenkov performance in separating between particle species. Efficiency is based on a photoelectron cut greater than 1.5.

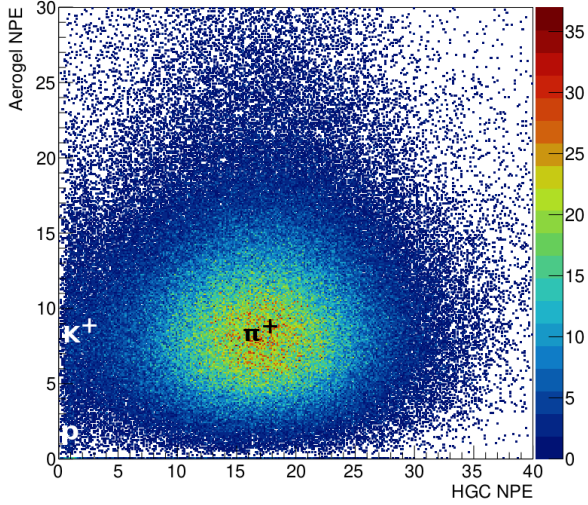


Figure 59: Demonstration of the particle identification capability of the Heavy Gas Cherenkov. Pictured is the separation between  $\pi^+$ ,  $K^+$  and proton at the 8.186 GeV beam energy and 6.053 GeV/c SHMS central momentum. The refractive indexes of HGC and aerogel Cherenkov detectors are 1.00143 and 1.011, respectively.

of +5.05 GeV/c<sup>2</sup>. Particle identification was performed by a cut on the aerogel Cherenkov detector and the normalized calorimeter energy. The spectrum obtained for the  $\pi/K$  separation is shown in Figure 59. This figure illustrates the broad distribution of NPE produced by  $\pi$ , fit with the red curve, which are above their momentum threshold. At the lower end of the NPE axis, there is a very large number of events producing no light, or just the SPE. These events correspond to  $K$  since they are below the momentum threshold to produce Cherenkov light. The presence of the SPE is likely due to  $\delta$ -rays, or knock-on  $e^-$ , a phenomenon where  $K$  can ionize the Cherenkov media and produce  $e^-$  which produce Cherenkov radiation. The vertical blue line indicates the NPE threshold, above which events are identified as  $\pi$ , below which are  $K$ . The summary of the particle identification efficiency and contamination is shown in Table 5.

Lastly, measurements of the  $\pi$  efficiency across a variety of momentum settings can be used to verify the index of refraction of the Cherenkov media. The relationship between  $\pi$  efficiency and momentum is fit with the equation [21]

$$\eta_{HGC} = 1 - e^{-(p-p_o)/\Gamma}, \quad (11)$$

where  $\eta_{HGC}$  is the detector efficiency,  $p$  is the momentum of the  $\pi$ , and  $p_o$  and  $\Gamma$  are free parameters. Data taken in the range of 2.53 GeV/c to 5.05 GeV/c with the HGC filled with C<sub>4</sub>F<sub>10</sub> yields an index of refraction

of  $n = 1.001 \pm 0.002$ . This is in agreement with the accepted value of  $n = 1.00143$  [22].

### 6.3.2. SHMS Aerogel Performance

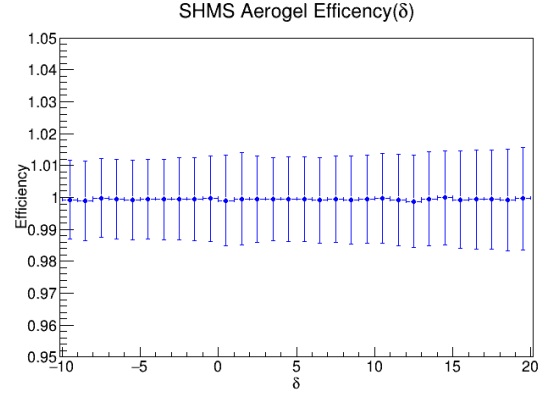


Figure 60: The efficiency of the aerogel is plotted over a range of  $\delta$ . This efficiency is taken at a beam energy of 6.2 GeV for an SHMS central momentum of 3.486 GeV/c. The refractive index of the aerogel detector is 1.015.

PID Configuration	Efficiency	Contamination
$K^+/p$	99.94%	1000 : 1

Table 6: Aerogel performance for kaon-proton separation with efficiency based off of cut greater than 1.5 photoelectrons.

The primary use of the aerogel Cherenkov detector in the SHMS is to distinguish between kaon and protons. A variety of aerogel tile refractive indices are used to reach a range of momenta. A cut greater than 1.5 photoelectron (NPE) cut is used to properly identify the particles. Figure 59 shows the particle identification of the Heavy Gas Cherenkov as well as the aerogel Cherenkov detector. This figure shows the importance of having both the Heavy Gass and the aerogel Cherenkov detectors as the kaon and proton would be indistinguishable without the aerogel.

In order for clean samples of the kaon, a high detector efficiency in the aerogel is required. The efficiency is determined by

$$\eta_{aero} = \frac{K^+ \text{ detected with aerogel signal}}{K^+ \text{ detected without aerogel signal}}, \quad (12)$$

where the detector efficiency is represented by  $\eta_{aero}$ . The efficiency of the aerogel detector can be seen in table 6. It is clear that the aerogel has a very high efficiency as required but this efficiency also runs over the

full range of  $\delta$  as seen in figure 60. This, plus the ability to change refractive indices, allows for terrific kaon identification over a wide range of kinematics.

### 6.3.3. Performance of SHMS calorimeter

#### Material on the gain stability/consistency to be added (resolution versus run number for a time period, or mip peak position versus run number).

The performance of the SHMS calorimeter under the beam conditions was tested first time during 12 GeV Hall C Key Performance Parameter Run in spring of 2017. As part of the SHMS detector package the calorimeter was commissioned in the Hall C fall run period of the same year. The first experimental data with use of the calorimeter is being collected for series of the first 12 GeV Hall C experiments: E12-10-002 ( $F_2$  structure function at large  $x$ ) [56], E12-06-107 (Search for Color Transparency) [59], E12-10-008 (EMC effect) [57], E12-10-003 (Deuteron Electro-Disintegration) [58], E12-09-017 ( $P_t$  dependence of SIDIS cross section) [60], E12-09-002 (Precise  $\pi^+/\pi^-$  ratios in SIDIS) [61] and E12-09-011 (L/T separated  $p(e, e'K)$  factorization test) [42]. The early analyses of the calorimeter data demonstrate satisfactory performance of the detector in terms of resolution and PID capabilities (fig. 61).

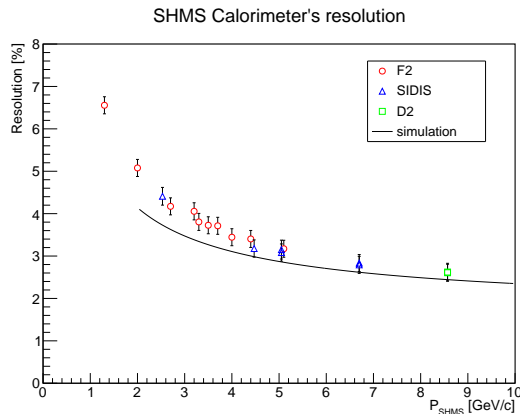


Figure 61: Resolution of the SHMS calorimeter from calibrations of runs from the Spring 18 run period. The solid line is result from the early simulations. [This figure is not final.]

## 7. Conclusion

- The SHMS has been in service for a number of years and has demonstrated itself to be both reliable and stable with respect to its ion optics. Numerous experiments have been published.

- Hall-C Collaboration, JLab Internal Document - (2002).
- Physics & Instrumentation with 6-12 GeV Beams, a Thomas Jefferson National Accelerator Facility report, S. Dytman, H. Fenker and P. Roos, eds., June 1998.
- References to SHMS magnet conference papers and/or publications or tech-notes.
- I. Niculescu et al., Phys. Rev. Lett. 85 (2000) 1186;
- T. Kitagaki, et al., Phys. Rev. D 42 (1990) 1331; A. Bergier, et al., Z. Phys. C 5 (1980) (265), and references therein.
- J. R. Dunning et al., Phys. Rev. 141 (1966) 1286; R. Bilger, et al., Nucl. Inst. and Meth. A 457 (2001) 64; I. Lehmann, et al., Nucl. Instr. and Meth. A 530 (2004) 275; A. Klimenko, et al., Phys. Rev. C 73 (2006) 035212.
- The ALICE Transition Radiation Detector: Construction, operation, and performance, ALICE Collaboration, Nucl. Inst. and Meth. A 888 (2018) 88-127;
- The G0 Experiment, D. Androic, et al., Nucl. Inst. and Meth. A 646 (2011) 59-86;
- The HERMES Spectrometer, K. Ackerstaff, et al., Nucl. Inst. and Meth. A 417 (1998) 230-265;
- A forward magnetic spectrometer system for high-energy heavy-ion experiments, K. Shigaki, et al., Nucl. Inst. and Meth. A 438 (1999) 282-301;
- CLAS, B. Mecking, et al., Nucl. Inst. and Meth. A 503 (2003) 513-553;
- The aerogel threshold Cherenkov detector for the High Momentum Spectrometer in Hall C at Jefferson Lab, R. Asaturyan, et al., Nucl. Inst. and Meth. A 548 (2005) 364-374;
- The Aerogel Čerenkov counter for the SHMS magnetic spectrometer in Hall C at Jefferson Lab, T. Horn, et al., Nucl. Inst. and Meth. A 842 (2017) 28-47;
- T. Skwarnicki, NIM A553 (2005) 339-344; M. Artuso et al., NIM A558 (2006) 373-387.
- ASM Aerospace Specification Metals, 14112 Pontiaovoy Ave., Santa Fe Springs, CA.
- Sinclair Glass, 105 N. Wabash Ave., Hartford City, IN.
- W. Li, M.Sc. thesis, University of Regina, 2012.
- Corning International, 1 Riverfront Plaza, Corning, NY.
- Hamamatsu Photonics K.K., Electron Tube Division, 314-5 Shimokanzo, Iwata City, Ahizuoka Pref., Japan
- Evaporated Coatings Inc., 2365 Maryland Rd., Willow Grove, PA.
- E.J Brash et al, NIM A487 (2002) 346-352
- Ruggero Turra, CERN, (2009).
- Vijay Kumar, *Updated SHMS HGC Calibration Code*, JLab Hall C Document Database 1098-v1 (27 Oct 2020)
- Rayotek Scientific (<https://rayotek.com/>).
- Detector Technologies Group (CERN) (<https://ep-dep-dt.web.cern.ch/>).
- ET Enterprises (<http://et-enterprises.com/>).
- T. Horn, *SHMS Shielding Design*, JLab Hall C Document Database 392-v1 (19 Nov 2008); *Final SHMS Shielding Design*, JLab Hall C Document Database 595-v1 (24 Sept 2009)
- P. J. Griffin et al., *The role of thermal and fission neutrons in reactor neutron-induced upsets in commercial SRAMs*, IEEE NS Vol. 44, No. 6, Dec. 1997.
- C. I. Underwood, *The Single-Event-Effect Behaviour of Commercial-Off-The-Shelf Memory Devices - A Decade in the Low-Earth orbit*, IEEE Transactions on Nuclear Science Vol. 45, No. 3, June 1998.
- W. R. Leo, *Techniques for Nuclear and Particle Physics Experiments*, second edition, Springer Verlag Berlin, Heidelberg 1987, 1994
- J. F. Briesmeister (ed.), MCNP - A General Monte Carlo N-particle Transport Code Version A, LA-12625-M, Los Alamos

- National Laboratory, Los Alamos, New Mexico (1993). 2320
- [32] S. Wood, private communication (2008). 2321
- [33] M. Jones *et al.*, private communication (2008). 2322
- [34] Birenbaum *et al.*, Phys. Rev. **C51**, (1995) 3496 2323
- [35] D. Marsh, *Particle Practice Concrete Products* **Vol. 117**, no. 2 2324  
(2014) 40. 2325
- [36] T. Horn, et al., The Aerogel Čerenkov detector for the SHMS 2326  
magnetic spectrometer in Hall C at Jefferson Lab, Nucl. In- 2327  
strum. Meth. A842 (2017) 28–47. [arXiv:1607.05264](https://arxiv.org/abs/1607.05264), doi: 2328  
[10.1016/j.nima.2016.10.039](https://doi.org/10.1016/j.nima.2016.10.039). 2329
- [37] Gore, W. L. & Associates INC., "", <http://www.gore.com>. 2330
- [38] Millipore Corporation, 80 Ashly Road, Bedford, MA 01730, "", 2331  
<http://www.millipore.com/>. 2332
- [39] I. Adachi, et al., Study of highly transparent silica aerogel as a 2333  
RICH radiator, Nucl. Instrum. Meth. A553 (2005) 146–151. 2334  
doi:[10.1016/j.nima.2005.08.022](https://doi.org/10.1016/j.nima.2005.08.022). 2335
- [40] E. Aschenauer, et al., Optical characterization of  $n = 1.03$  2336  
silica aerogel used as radiator in the RICH of HERMES, 2337  
Nucl. Instrum. Meth. A440 (2000) 338–347. doi:[10.1016/](https://doi.org/10.1016/S0168-9002(99)00923-7) 2338  
[S0168-9002\(99\)00923-7](https://doi.org/10.1016/S0168-9002(99)00923-7). 2339
- [41] Horn T., Huber G.M., and others, "scaling study of the l-t sepa- 2340  
rated pion electroproduction cross section at 11 gev", approved 2341  
Jefferson Lab 12 GeV Experiment (2007). 2342
- [42] T. Horn, G. M. Huber, P. Markowitz, et al., Spokespersons, 2343  
Studies of the L-T Separated Kaon Electroproduction Cross 2344  
Section from 5-11 GeV JLab proposal E12-09-011. . 2345
- [43] Bosted P., Ent R., Kinney E., Mkrtychyan, H., and others, "Mea- 2346  
surement of the Ratio  $r = \sigma_l/\sigma_t$  in Semi-Inclusive Deep- 2347  
Inelastic Regimes", approved Jefferson Lab 12 GeV Experiment 2348  
(2006). 2349
- [44] R. Asaturyan, et al., The aerogel threshold Cerenkov detector 2350  
for the high momentum spectrometer in Hall C at Jefferson Lab, 2351  
Nucl. Instrum. Meth. A548 (2005) 364–374. [arXiv:physics/](https://arxiv.org/abs/physics/0411147) 2352  
[0411147](https://arxiv.org/abs/physics/0411147), doi:[10.1016/j.nima.2005.04.058](https://doi.org/10.1016/j.nima.2005.04.058). 2353
- [45] H. Mkrtychyan *et al.*, Nucl. Instrum. Meth. A **719** (2013) 85-100. 2354
- [46] H. Avakian *et al.*, Nucl. Instrum. Meth. A **378** (1996) 155-161. 2355
- [47] H. Avakian *et al.*, Nucl. Instrum. Meth. A **417** (1998) 69-78. 2356
- [48] J. Alcorn *et al.*, Nucl. Instrum. Meth. A **522** (2004) 294. 2357
- [49] Lytcarino factory of optical glasses, 140061, Lytkarino, 2358  
Moskow region, Russia. 2359
- [50] T. Amatuni, G. Kazaryan, H. Mkrtychyan, V. Tadevosyan and W. 2360  
Vulcan, Nucl. Instr. Meth. A **374**, 39-47 (1996). 2361
- [51] C. Zorn, private communication. 2362
- [52] S. Agostinelli *et al.*, GEANT4—a simulation toolkit. Nucl. In- 2363  
strum. Meth. A **506** (2003) 250-303; J. Allison *et al.*, EEE 2364  
Transactions on Nuclear Science **53**, No.1, (2006) 270-278. 2365
- [53] John Apostolakis *et al.*, Progress in hadronic physics model- 2366  
ing in GEANT4. XIII Int. Conf. on Calorimetry in High En- 2367  
ergy Physics. (CALO2008); J. of Phys. Conf. Series **160** (2009) 2368  
012073; J. Apostolakis *et al.*, Hadronic Shower Shape Studies 2369  
in GEANT4, CERN-LCGAPP-2007-02. 2370
- [54] M. Born, E. Wolf. Principles of Optics. Pergamon Press, 1965. 2371
- [55] Ts. Amatuni, On the calibration of segmented full absorption 2372  
calorimeters. Unpublished. 2373
- [56] Precision measurements of the  $F_2$  structure function at large  $x$  2374  
in the resonance region and beyond, JLab Proposal E12-10-002, 2375  
S. Malace, M. Christy, C. Keppel, M. Niculeclu spokespersons. 2376
- [57] Detailed studies of the nuclear dependence of  $F_2$  in light nuclei, 2377  
Jlab Proposal E12-10-008, D. Gaskell, J. Arrington, A. Daniel, 2378  
N. Fomin spokespersons. 2379
- [58] Deuteron Electro-Disintegration at Very High Missing Mo- 2380  
mentum, JLab Proposal E12-10-108, W. Boeglin, M. Jones 2381  
spokespersons. 2382
- [59] D. Dutta, R. Ent, et al. Spokespersons, "The Search for Color 2383  
Transparency at 12 GeV", approved Jefferson Lab 12 GeV Ex- 2384  
periment (2006). 2385
- [60] R. Ent, P. Bosted, E. Kenney, H. Mkrtychyan spokespersons, 2386  
"Transverse Momentum Dependence of Semi-Inclusive Pion 2387  
Production", approved Jefferson Lab 12 GeV Experiment 2388  
(2009). 2389
- [61] Precise Measurement of  $\pi^+/\pi^-$  Ratios in Semi-inclusive Deep 2390  
Inelastic Scattering Part I: Charge Symmetry violating Quark 2391  
Distributions, JLab Proposal E12-09-002, K. Hafidi, D. Dutta, 2392  
D. Gaskell spokespersons. 2393
- [62] *Hall A Analyzer*, <https://hallaweb.jlab.org/podd/>. 2394
- [63] Rene Brun and Fons Rademakers, *ROOT - An Object Oriented 2395  
Data Analysis Framework*, Proceedings AIHENP'96 Workshop, 2396  
Lausanne, Sep. 1996, Nucl. Instrum. Meth. A **389** (1997) 81-86. 2397  
See also <http://root.cern.ch/>. 2398
- [64] Experimental Physics and Industrial Control System (EPICS), 2399  
<https://epics-controls.org/>. 2400
- [65] CEBAF Online Data Acquisition System (CODA), [https://](https://coda.jlab.org/) 2401  
[coda.jlab.org/](https://coda.jlab.org/). 2402
- [66] Jefferson Lab F250 Flash ADC module, [https://coda.jlab.](https://coda.jlab.org/) 2403  
[org/](https://coda.jlab.org/). 2404
- [67] CAEN v1190 Time to Digital Converter, [https://www.caen.](https://www.caen.it/products/v1190a-2esst/) 2405  
[it/products/v1190a-2esst/](https://www.caen.it/products/v1190a-2esst/). 2406
- [68] Jefferson Lab Scientific Computing, [https://scicomp.](https://scicomp.jlab.org/) 2407  
[jlab.org](https://scicomp.jlab.org/). 2408
- [69] FIXME: Hall C HMS reference?. 2409
- [70] V. Tvaskis, M. Christy, *et al.*, Phys. Rev. Lett. **98**, 142301 (2007) 2410  
doi:10.1103/PhysRevLett.98.142301 [arXiv:nucl-ex/0611023 2411  
[nucl-ex]]. 2412
- [71] J. Volmer *et al.* [Jefferson Lab F(pi)], Phys. Rev. Lett. **86**, 1713- 2413  
1716 (2001) doi:10.1103/PhysRevLett.86.1713 [arXiv:nucl- 2414  
ex/0010009 [nucl-ex]]. 2415
- [72] T. Horn *et al.* [Jefferson Lab F(pi)-2], Phys. Rev. Lett. 2416  
**97**, 192001 (2006) doi:10.1103/PhysRevLett.97.192001 2417  
[arXiv:nucl-ex/0607005 [nucl-ex]]. 2418
- [73] T. Navasardyan, *et al.* Phys. Rev. Lett. **98**, 022001 (2007) 2419  
doi:10.1103/PhysRevLett.98.022001 [arXiv:hep-ph/0608214 2420  
[hep-ph]]. 2421
- [74] D. Abbott, *et al.*, Phys. Rev. Lett. **80**, 5072-5076 (1998) 2422  
doi:10.1103/PhysRevLett.80.5072. 2423
- [75] K. Garrow, *et al.*, Phys. Rev. C **66**, 044613 (2002) 2424  
doi:10.1103/PhysRevC.66.044613 [arXiv:hep-ex/0109027 2425  
[hep-ex]]. 2426
- [76] N. Fomin, *et al.*, Phys. Rev. Lett. **105**, 212502 (2010) 2427  
doi:10.1103/PhysRevLett.105.212502 [arXiv:1008.2713 [nucl- 2428  
ex]]. 2429
- [77] N. Fomin, *et al.*, Phys. Rev. Lett. **108**, 092502 (2012) 2430  
doi:10.1103/PhysRevLett.108.092502 [arXiv:1107.3583 [nucl- 2431  
ex]]. 2432